Petroleum Science 23 (2026) 2452–2466

Contents lists available at ScienceDirect

Petroleum Science

journal homepage: www.keaipublishing.com/en/journals/petroleum-science

Original Paper

Evolution of multistage dolomitization fluids in the Upper Ediacaran Qigebrak Formation, northern Tarim Basin, China: Effects on reservoir formation

Pan Tang [a], Xiang-Rong Yang [b], Feng Guo [a], You-Jun Tang [a,*], Yuan-Zheng Wang [c], Bo Yang [d], Wen-Yang Wang [d], Dai-Zhao Chen [e,**]

[a] Hubei Key Laboratory of Petroleum Geochemistry and Environment, College of Resources and Environment, Yangtze University, Wuhan, 430100, Hubei, China
[b] School of Geosciences, Yangtze University, Wuhan, 430100, Hubei, China
[c] Wuxi Research Institute of Petroleum Geology, SINOPEC, Wuxi, 214151, Jiangsu, China
[d] Key Laboratory of Deep Petroleum Intelligent Exploration and Development, Institute of Geology and Geophysics, Chinese Academy of Sciences, Beijing, 100029, China
[e] State Key Laboratory of Lithospheric and Environmental Coevolution, Institute of Geology and Geophysics, Chinese Academy of Sciences, Beijing, 100029, China

ARTICLE INFO

Article history:
Received 1 July 2025
Received in revised form
24 October 2025
Accepted 10 March 2026
Available online 14 March 2026

Edited by Xiu-Fang Hu

Keywords:
Multistage dolomitization
Deep-buried
Upper Ediacaran
Reservoir evolution

ABSTRACT

The deep-buried dolomites of the Upper Ediacaran Qigebrak Formation in the Tarim Basin possess substantial hydrocarbon potential. Although diagenetic processes, particularly dolomitization, are recognized as critical for reservoir evolution in this formation, their specific impacts on reservoir quality remain poorly understood. This study utilizes newly acquired petrographic, stable isotope, and radiogenic isotope data, integrated with carbonate U–Pb ages and temperature data, to elucidate the relationship between dolomitization processes and reservoir evolution in the Qigebrak Formation. Seven distinct dolomite phases were identified: dolomicrite (D1), very fine crystalline dolomite (D2), fine crystalline dolomite (D3), fibrous dolomite cement (D4), bladed dolomite cement (D5), fine to medium crystalline dolomite cement (D6), and coarse crystalline saddle dolomite cement (D7). D1 and D2 exhibit $\delta^{13}C$ and $^{87}Sr/^{86}Sr$ ratios consistent with coeval Ediacaran seawater, indicating an initial syngenetic dolomitization event in restricted lagoon/tidal flat environments. This event formed via near-surface dolomitization driven by the reflux of slightly evaporative seawater. D4 and D5 also precipitated in near-surface settings under seawater dolomitization conditions, but their depleted $\delta^{13}C$ and $\delta^{18}O$ values with elevated $^{87}Sr/^{86}Sr$ ratios suggest the involvement of meteoric water in the precipitation process. In contrast, most D3 and D6 were formed through burial dolomitization at elevated temperatures. D7 originated from hydrothermal dolomitization at 135–150 °C, characterized by progressively depleted $\delta^{18}O$ ratios with increasing burial depth and the mixing of ^{87}Sr-enriched hydrothermal fluids. Notably, early syngenetic dolomitization preserved primary pores in the Qigebrak Formation despite long-term burial, whereas later burial and hydrothermal dolomitization primarily adjusted the pre-existing pore systems. This study enhances our understanding of multistage dolomitization processes in the Qigebrak Formation and provides insights for future exploration of Precambrian successions.

1. Introduction

Dolomite reservoirs constitute over half of the world's carbonate oil and gas reservoir rocks, contributing substantially to global petroleum resource production (Warren, 2000; Ahmad et al., 2022; Rahim et al., 2022). In the past decade, deep-buried Precambrian dolomite reservoirs have emerged as critical targets

* Corresponding author.
** Corresponding author.
E-mail addresses: tyj@yangtzeu.edu.cn (Y.-J. Tang), dzh-chen@mail.iggcas.ac.cn (D.-Z. Chen).
Peer review under the responsibility of China University of Petroleum (Beijing).

https://doi.org/10.1016/j.petsci.2026.03.022

for hydrocarbon exploration (Grotzinger and Al-Rawahi, 2014; Frolov et al., 2015; Zhou et al., 2020; Jin et al., 2025). For instance, the Upper Ediacaran dolomites in Sichuan Basin, China contain the world's largest volume of unproven gas resources, even though they have been buried at depths exceeding 7 km (Jiang et al., 2023). Similarly, recent explorations in Tarim Basin, China have achieved significant breakthroughs: the Luntan-1 and TS-5 wells revealed gas-bearing dolomite reservoirs in the Qigebrak Formation (Yang et al., 2020a), suggesting promising potential for hydrocarbon exploration in such deep-buried geological settings.

The dolomite reservoirs of the Ediacaran Qigebrak Formation display remarkable complexity and heterogeneity, previous studies have shown the Qigebrak Formation reservoirs in the northern Tarim Basin are predominantly composed of dolomicrobialites, dolomudstone and crystalline dolomites with various dolomite cements (Li et al., 2015, 2021a; Shi et al., 2017). These investigations have focused on sedimentary facies, reservoir characterization, and diagenetic processes in the Qigebrak dolomite reservoirs (Zhu et al., 2021; Tang et al., 2022; Zhao et al., 2023). More recently, several studies have addressed the timing and mechanisms of dolomitization in this formation. For example, Yang et al. (2020b) conducted U–Pb dating on multiphase dolomites from outcrop samples in the northwestern Tarim Basin, constraining the formation of the host dolomite rocks to between 576.0 ± 16.0 Ma and 560.0 ± 26.0 Ma. Zheng et al. (2021a) attributed the origin of matrix dolomites to seepage-reflux and evaporative dolomitization processes, while Zhao et al. (2024) classified the dolomites into several diagenetic phases and investigated the corresponding dolomitizing fluids. Nevertheless, the evolutionary pathways of these dolomitizing fluids and their impact on reservoir development remain poorly constrained.

Furthermore, the origin of pores in the Qigebrak dolomite reservoirs remains a subject of debate. A lack of detailed petrographic evidence has led some researchers to challenge the hypothesis of deep-buried dolomite dissolution and porosity generation in this basin (Yan et al., 2019; Shang et al., 2020; Chen et al., 2023). Additionally, knowledge gaps persist in understanding the sedimentary facies and early-stage dolomitization of the Qigebrak Formation, and recent work suggests these factors may be more critical for the reservoir formation than deep burial dissolution processes (Zheng et al., 2023). Therefore, evaluating the coupled effects of dolomitization fluid evolution across different stages and their influence on the formation and modification of ultra-deep carbonate reservoirs is of vital importance.

To reconstruct reservoir evolution in the Upper Ediacaran Qigebrak Formation, this study integrates analysis of dolomitization processes, diagenetic events, and tectonic history. We identify key factors governing pore creation and preservation during diagenesis. Multistage dolomitization, diagenetic fluid sources, and their influence on reservoir evolution are constrained through detailed petrological and geochemical analyses. Specifically, this research addresses three critical questions regarding the Upper Ediacaran Qigebrak Formation: (1) What are the main petrologic and geochemical characteristics of the different types of dolomites? (2) What were the dolomitization mechanisms of these dolomites? (3) How did different diagenetic fluids contribute to the reservoir formation? The findings of this study extend beyond the Tarim Basin, providing a theoretical framework for hydrocarbon exploration in analogous deep-buried dolomite reservoirs globally, and offering insights into reservoir quality assessment with similar geological settings.

2. Geological background

The Tarim Basin, an intracratonic basin, is bounded by the Tianshan Mountains to the north, the Kunlun Mountains to the southwest, and the Altun Mountains to the southeast (Fig. 1(a); Wu et al., 2017). Developed on a Precambrian basement, this large-scale superimposed basin formed through complex tectonic processes (Turner, 2010; Shen et al., 2022b). Its geological evolution began as a rift basin in the late Neoproterozoic, transitioning to a cratonic marine basin before evolving into a non-marine basin during the Mesozoic (Fig. 1(a); Jia, 1999; Zhang et al., 2013; Shen et al., 2022b). As a result of these complex geological histories, the basin is divided into distinct structural units (Fig. 1(a)). The studied outcrops (LKG and SA) and wells (LT-1, QT-1 and XH-1) are situated in the northern Tarim Basin (Fig. 1(a)), and the study area was characterized by a shallow-water carbonate platform during the Late Ediacaran (Zheng et al., 2021a; Wang et al., 2022; Zhao et al., 2023).

The Ediacaran strata, in ascending order, consist of the Sugaitebrak (Z_1s) and Qigebrak (Z_2q) formations (Fig. 1(b)). Detailed core and outcrop observations reveal that three third-order sequences can be recognized in these strata (Shi et al., 2016; Fig. 1(b)). The Lower Ediacaran Sugaitebrak Formation is characterized by a mixed siliciclastic–carbonate platform deposition, composed of interbedded carbonate and siliciclastic rocks (Wang et al., 2022; Huang et al., 2025; Fig. 1(b)). Overlying the Sugaitebrak Formation, the Qigebrak Formation is dominated by massive dolostones (Bao et al., 2022; Fig. 1(b)). Extensive subaerial exposure during the Late Ediacaran resulted in a paraconformity between the Qigebrak Formation and the Lower Cambrian Yuertusi Formation (He et al., 2018; Fig. 1(c)). In the study area, the Qigebrak Formation ranges in thickness from 145 m to 175 m, with microbial dolostones constituting over 75% of its volume (Fig. 2). Microbial fabrics, such as stromatolites, microbial laminites, and spongy textures, are commonly observed in these Qigebrak dolostones (Fig. 2).

The burial histories of the Qigebrak Formation from Well LT-1 and the Keping outcrop are illustrated in Fig. 3. In the well LT-1, the Qigebrak Formation underwent continuous burial to ~4.5 km during the early Permian. Subsequent uplift in the Triassic shallowed the strata to ~4 km, after which renewed burial reached the current depth of ~8.7 km. In contrast, the Keping area attained a maximum burial depth of ~4.5 km in the early Carboniferous, followed by rapid uplift to ~3.5 km in the Permian. Thereafter, after a period of minor subsequent burial, the strata gradually uplifted to form the present-day outcrops (Chang et al., 2011).

3. Samples and methods

Samples utilized in this study were collected from two outcrop sections (LKG, SA) and three drilled wells (LT-1, QT-1 and XH-1) from the Qigebrak Formation. To cover the main lithofacies, samples were obtained from various sedimentary facies (e.g., tidal flats and lagoons), and a total of 160 samples from both outcrops and drilling cores were prepared as thin sections for analysis. After the observation under transmitted light optical microscopy, these thin sections were then analyzed with cathodoluminescence (CL) microscopy. The CL analysis was carried out using a Reliotron Relion III model, with an acceleration voltage of 5–8 kV and a gun current of 300–400 μA. Combined with core descriptions and scanning electron microscopy (SEM), these observations characterized sedimentary structures, dolomite matrix and cement types, lithofacies, and paragenetic sequences. Moreover, we assembled geochemical data, such as carbon and oxygen isotopes, strontium

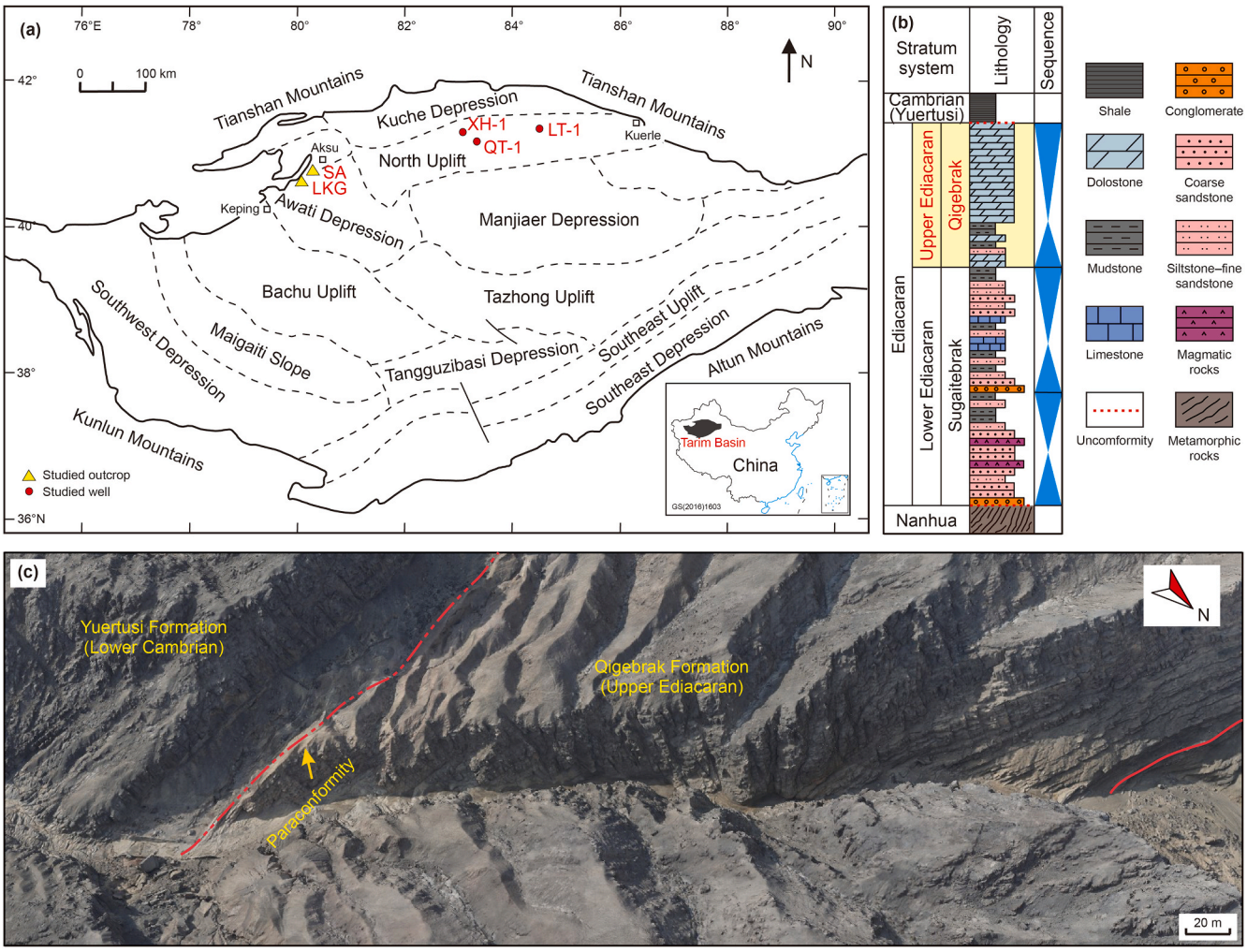

Fig. 1. **(a)** Geological map depicting the locations and study area of the Tarim Basin, modified after Zhu et al. (2015); **(b)** stratigraphy, lithology and sequences of the Ediacaran strata in the northern Tarim Basin, modified after Shi et al. (2016); **(c)** photograph showing the plan view of Qigebrak and Yuertusi formations taken from an unmanned aerial vehicle.

isotopes, and temperature data obtained from fluid inclusions and clumped isotope measurements on diverse dolomite phases.

Geochemical analysis samples were collected via micro-drilling using a hand-held dental drill under microscopic guidance. A total of 41 samples were analyzed for carbon and oxygen stable isotopic compositions. For $\delta^{13}C$ and $\delta^{18}O$ measurements, approximately 4 mg of each sample was subjected to reaction with phosphoric acid for 10 h at 90 °C using the conventional acid bath technique (Land, 1980). The evolved CO_2 was analyzed using a Finnigan-MAT 252 mass spectrometer (Vahrenkamp and Swart, 1994). Results are reported in per mil (‰) relative to the Vienna Pee Dee Belemnite (VPDB) standard. Duplicate analyses ($n = 10$) exhibited typical 1σ uncertainties of <0.15‰ for $\delta^{13}C$ and <0.20‰ for $\delta^{18}O$. All analytical procedures were performed at the Stable Isotope Geochemistry Laboratory of the Institute of Geology and Geophysics, Chinese Academy of Sciences (IGGCAS).

Strontium isotope ratios ($^{87}Sr/^{86}Sr$) of various dolomite types from 21 representative samples were analyzed at IGGCAS following the methodology of Liu et al. (2021). Microdrilled dolomite samples (40–50 mg) were dissolved in 0.2 mol/L HCl at 80 °C for 4 h. The resulting solution was processed through an ion-exchange column to isolate strontium, followed by $^{87}Sr/^{86}Sr$ measurement using a Finnigan MAT-262 thermal ionization mass spectrometer. Strontium isotope ratios were calibrated relative to the NBS-987 standard, which yielded an average value of 0.7103. The standard deviation (2σ) of $^{87}Sr/^{86}Sr$ during the determination was less than 0.000024.

Temperature data were obtained through fluid inclusion (FI) and clumped isotope analyses. A total of 88 samples underwent analysis of fluid inclusions (FIs) to determine the homogenization temperatures and salinities of aqueous FIs. The salinity (expressed in wt.% NaCl equivalent) was computed from ice melting temperatures (T_m ice) by applying the equation proposed by Bodnar (1993). Special attention was given to fluid inclusion assemblages (FIAs) along growth zones, as these assemblages represent genetically related FI groups in petrology (Goldstein and Reynolds, 1994). The FI measurements were carried out using a Linkam THMSG 600 cooling and heating stage, which offered a precision of 0.1 °C. This stage was calibrated using synthetic pure water, CO_2 inclusions, and appropriate pressure corrections were applied to the FI groups.

Clumped isotope analyses were performed on 36 samples using the methodology described by Wang et al. (2016). Raw data underwent nonlinear corrections using standards ETH1–ETH4, whereas P1 (coral) and NB-4 (marble) served as working standards to minimize errors during sample preparation and analysis. Sample results were converted to Δ47 values in the carbon dioxide equilibrated scale (CDES), which is considered the absolute

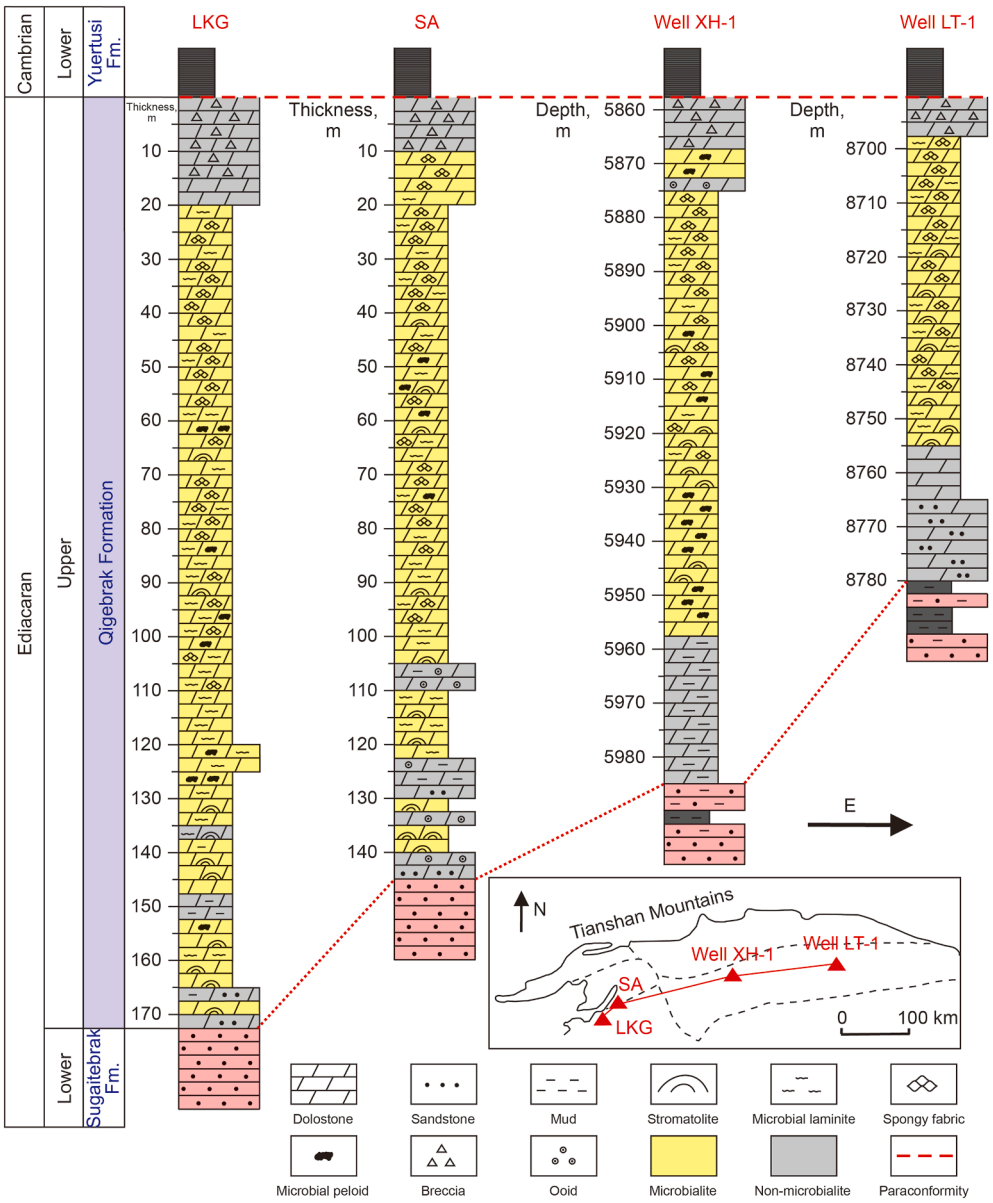

Fig. 2. Lithological columns of the Upper Ediacaran Qigebrak Formation in the study area.

reference system (Dennis and Schrag, 2010; Dennis et al., 2011). For the correlation between dolomite mineral formation temperature and Δ47 values, we refer to the formula proposed by Bernasconi et al. (2018). These analyses were also conducted at IGGCAS.

4. Results

4.1. Petrography

Diagenetic products such as dolomite and calcite are common throughout the Qigebrak Formation. In contrast, quartz, bitumen, and minor clay minerals occur locally. Specifically, based on the crystal size, distribution pattern and crystal boundary morphology (Gregg and Sibley, 1984; Guo et al., 2020), seven types of dolomite were distinguished: three types of matrix dolomites (D1 to D3) and four types of dolomite cements (D4 to D7). The matrix dolomites occur in the host dolostones and can be further subdivided into dolomicrite (D1), very fine crystalline dolomite (D2) and fine crystalline dolomite (D3). In comparison, the dolomite cements were found in the vugs and pores of the Qigebrak Formation, with four distinct types recognized: fibrous dolomite cement (D4), bladed dolomite cement (D5), fine to medium crystalline dolomite cement (D6) and coarse crystalline saddle dolomite cement (D7).

4.1.1. Dolomites

Dolomicrite (D1). This type of dolomite commonly occurs in thin-bedded outcrops and replaced restricted lagoonal facies (Fig. 4(a)). Microscopically, the D1 dolomite consists of very fine crystals with sizes ranging from 2 μm to 5 μm. Additionally, it generally occurs as subhedral to non-planar dolomite crystals, and low-amplitude stylolites are locally observed in the thin sections (Fig. 4(b)).

Very fine crystalline dolomite (D2). D2 is widely distributed throughout the Qigebrak Formation. This dolomite type typically displays microbial-like fabrics such as microbial laminite (Fig.

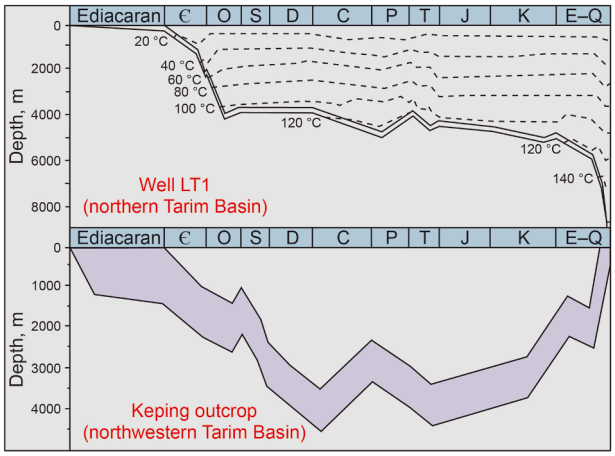

Fig. 3. Burial history of the Qigebrak Formation in the well LT-1 and Keping outcrop area, modified after Chang et al. (2011) and Zhao et al. (2024).

4(c)), stromatolites, and spongy-like fabrics (Fig. 4(d)). Microscopically, it consists of very fine crystals (typically 5–20 μm) and generally displays planar-e to planar-s crystal rhombs (Fig. 4(d)).

Fine crystalline dolomite (D3). D3 dolomite accounts for approximately 15% of the total dolostones. This type is distinguished by the complete replacement of primary sedimentary fabrics (Fig. 4(e)), consisting of nonplanar-a dolomite crystals with crystal sizes ranging from 50 μm to 200 μm (Fig. 4(f)). Notably, some D3 crystals exhibit undulatory extinction under cross-polarized light.

Fibrous dolomite cement (D4) and bladed dolomite cement (D5). D4 and D5 occur as cement crusts in sheet cavities in the tidal flat facies of the Upper Qigebrak Formation (Fig. 5(a)–(d)). Accounting for approximately 30% (based on visual estimation of thin sections), D4 forms isopachous crusts around grains. It commonly occurs in the D2 matrix and displays crystal lengths ranging from millimeter to centimeter scale (Fig. 5(a) and (b)). Notably, D5 overgrows D4 without optical continuity, characterized by bladed textures and associated residual pores (Fig. 5(c)).

Fine to medium crystalline dolomite cement (D6). D6 commonly occurs as pore-filling cement in the D2 dominated host rock of the Qigebrak Formation (Fig. 5(d) and (e)). In some sections, D6 often occludes most of the pre-existing pores and postdates the first-stage cement D4 (Fig. 5(d)). Composed of fine-to medium-crystalline planar-s to nonplanar-a dolomite rhombs, D6 displays a relatively unimodal crystal size distribution ranging from 50 μm to 400 μm (Fig. 5(d) and (e)).

Coarse crystalline saddle dolomite cement (D7). D7 dolomite is frequently observed in fractures and vugs associated with D6 (Fig. 5(e)), calcite, and quartz. Composed of coarsely crystalline, nonplanar-a dolomite rhombs (crystal sizes 500–800 μm), it grows at pore centers and occasionally overlies D6 (Fig. 5(e)). D7 crystals exhibit curved crystalline faces and undulose extinction (Radke and Mathis, 1980).

4.1.2. Other diagenetic products

Quartz. Vugs, pores, and fractures in the Qigebrak Formation are frequently occluded by quartz cements with crystal sizes of ~100–800 μm (Fig. 5(c)). These quartz cements often occur in association with coarse saddle dolomite cement (D7), calcite cements, and fluorite in the pore spaces of carbonate reservoirs.

Calcite. Calcite cements are predominantly observed in the upper part of the Qigebrak Formation, categorized into two main types: (1) mega-crystalline calcite cement, which is commonly observed in vugs and paleocaves in the uppermost Qigebrak Formation, occurring associated with karst breccias (Fig. 5(f)). The calcite crystal size is between 800 μm and 10 cm; (2) mosaic calcite cement, characterized by crystal sizes of 50–200 μm, commonly filling pore spaces (Fig. 5(g)).

Bitumen. Bitumen occurs locally in the uppermost Qigebrak Formation. In the SA section, it is associated with columnar stromatolites (Fig. 5(h)), which usually developed in the D2. Additionally, stylolites in the D2 matrix are filled with bitumen, indicating hydrocarbon migration pathways (Fig. 5(i)).

Although multiple diagenetic processes modified pore networks and influenced petrophysical properties of reservoirs in the Qigebrak Formation, this study focused primarily on dolomitization, as this process may be the dominant controlling factor. The paragenetic sequence of the Qigebrak Formation is well-constrained by copious petrographic observations, with detailed paragenetic sequences documented in Fig. 6. During the syndepositional to early-diagenetic stage, D1 and D2 were formed by pervasive dolomitization, and microbial fabrics were completely dolomitized during this process. By the terminal Ediacaran, the study area underwent uplift and subaerial exposure (Shang et al., 2020), triggering meteoric dissolution in the upper interval of the Qigebrak Formation. Subsequent to this dissolution event, the first and second generations of dolomite cements (D4 and D5) precipitated along the margins of pores and vugs. As burial depth increased, D3 and D6 were formed, and hydrocarbon started to migrate into pore spaces. During late diagenesis, fractures likely developed due to the release of tectonic stress. The subsequent precipitation of D7, quartz, and calcite further diminished the reservoir spaces.

4.2. Geochemistry

4.2.1. Stable carbon and oxygen isotope

The stable isotope (C and O) analysis results are presented in Fig. 7 and Table 1. D1 samples exhibit relatively positive $\delta^{13}C$ values ranging from 2.79‰ to 5.16‰ VPDB, with a narrow $\delta^{18}O$ range of −3.89‰ to −0.04‰ VPDB. These values largely overlap with the $\delta^{13}C$ (1.79‰–3.59‰ VPDB) and $\delta^{18}O$ (−4.79‰ to −0.72‰ VPDB) ranges of D2 samples. D3 samples show $\delta^{13}C$ values between 1.04‰ and 3.77‰ VPDB and $\delta^{18}O$ values from −7.76‰ to −2.35‰ VPDB. Early-diagenetic D4 and D5 dolomites display a narrow $\delta^{13}C$ range (0.35‰ to 3.16‰ VPDB) and have $\delta^{18}O$ values from −7.52‰ to 0.86‰ VPDB. In general, D4 and D5 isotopic values are lower than those of matrix dolomites (D1, D2, D3), though minor overlap exists (Fig. 7). D6 samples have a narrow $\delta^{13}C$ (0.06‰–1.83‰ VPDB) and $\delta^{18}O$ (−10.43‰ to −8.25‰ VPDB) range. D7 shows $\delta^{13}C$ of −0.30‰ to 1.79‰ VPDB and $\delta^{18}O$ of −12.64‰ to −9.81‰ VPDB. Calcite cements (CC) form a distinct group, characterized by predominantly negative $\delta^{13}C$ (−0.89‰ to 0.46‰ VPDB) and the lowest $\delta^{18}O$ values (−13.02‰ to −11.47‰ VPDB) among all samples.

4.2.2. Strontium isotope

The $^{87}Sr/^{86}Sr$ ratios of various carbonate minerals from the Qigebrak Formation are presented in Fig. 8 and Table 1. D1, D2, and D3 samples exhibit a narrow range of low $^{87}Sr/^{86}Sr$ values (0.708466 to 0.708940), with the exception of one D3 sample (0.710063). These values for most matrix dolomites align with the estimated seawater $^{87}Sr/^{86}Sr$ range (0.708464 to 0.709089) during the Late Ediacaran (Fig. 8; Zhang et al., 2020). D4 and D5 samples show relatively elevated ratios, with two D4 samples displaying highly radiogenic values (0.709670 and 0.710000). D6 and D7 exhibit significantly elevated $^{87}Sr/^{86}Sr$ ratios (0.709130 to 0.709625), while calcite cements (CC) show high values ranging from 0.709810 to 0.709848.

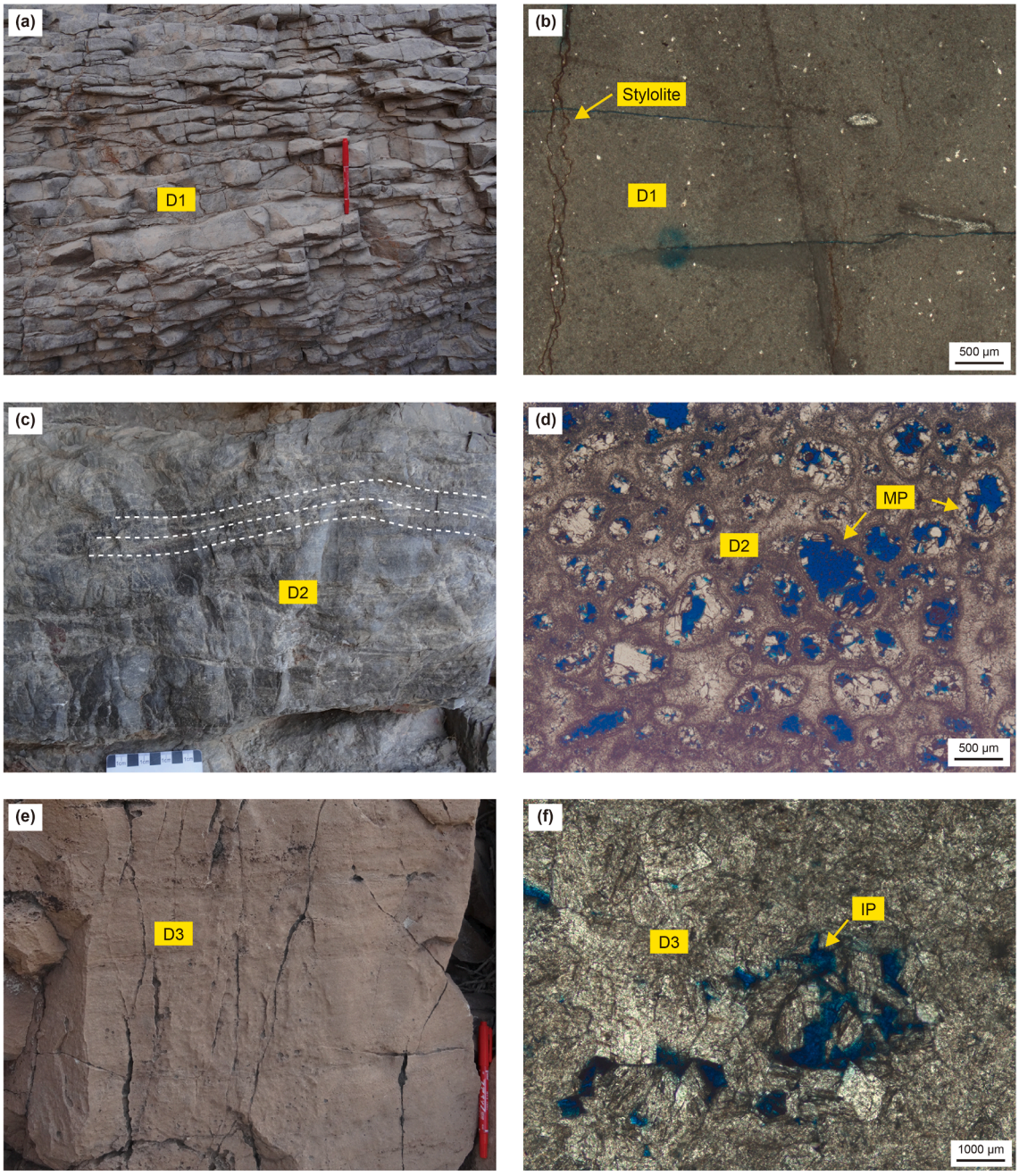

Fig. 4. Outcrop and photomicrographs showing the Qigebrak dolomite matrix. The pen in (a) and (e) is 15 cm long for scale. **(a)** Thin-bedded dolomicrites (D1) deposited in lagoon facies, outcrop, LKG section; **(b)** low-amplitude stylolite occurs associated with dolomicrites (D1), thin section, SA section; **(c)** abundant microbial laminae (dashed lines) developed in the very fine crystalline dolomite (D2), outcrop, LKG section; **(d)** spongy fabrics in the D2 with a large number of microbial-framework pores (MP), thin section, SA section; **(e)** medium-to thick-bedded fine crystalline dolomite (D3) without typical microbial fabrics, outcrop, SA section; **(f)** D3 shows nonplanar dolomite crystals with some residual intercrystalline pores (IP), thin section, LKG section.

4.2.3. Temperature data

Clumped isotope and fluid inclusion microthermometric data constrain different mineral temperatures in the Qigebrak Formation (Fig. 9), which reveal distinct formation temperatures.

Due to the difficulty in observing two-phase inclusions in early-formed dolomites, clumped isotope analyses were performed on these matrix dolomites (D1 to D3) and early-diagenetic dolomite cements (D4 and D5) (Shen et al., 2021). Results show that D1 and D2 exhibit relatively low precipitation temperatures (mostly <65 °C), consistent with near-surface diagenetic conditions. The $\delta^{18}O_{water}$ values of their corresponding dolomitization fluids are from 3.09‰ to 4.90‰ Vienna Standard Mean Ocean Water (VSMOW) (Fig. 10). In comparison, D3 dolomites have relatively higher temperatures (62 °C to 77 °C) and lower $\delta^{18}O_{water}$ values (0.99‰ to 2.88‰ VSMOW). D4 and D5 samples yield similar temperatures to those of matrix dolomites, varying from 60 °C to 68 °C, but have distinctly lower $\delta^{18}O_{water}$ values (−0.47‰ to −0.14‰ VSMOW) (Fig. 10).

For ancient dolomites, the ^{13}C–^{18}O bonds within carbonate crystals may undergo reordering through solid-state exchange reactions, potentially affecting the accuracy of measured clumped isotope temperatures (Stolper and Eiler, 2015; Li et al., 2021b). It is

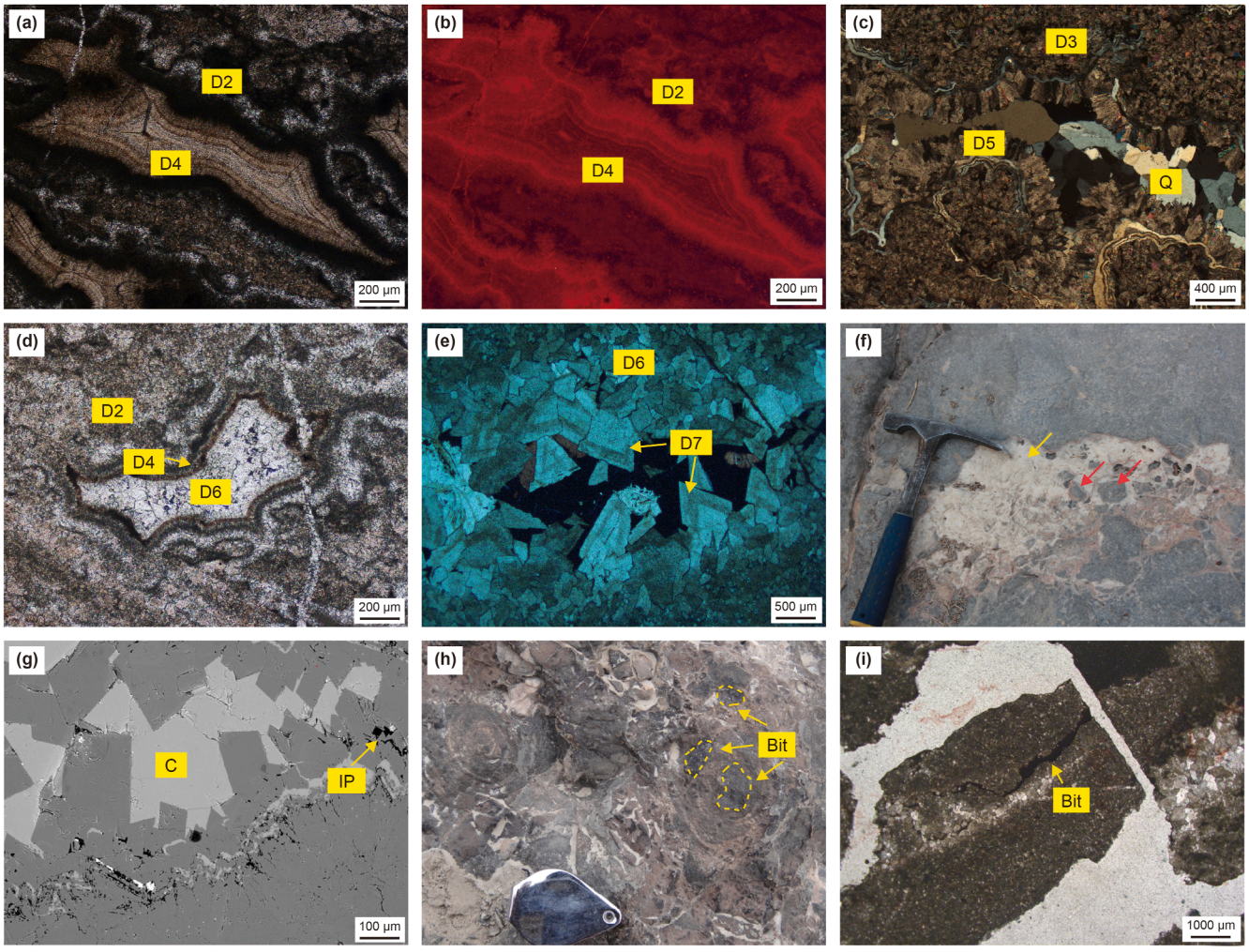

Fig. 5. Outcrop and photomicrographs showing the Qigebrak dolomite cement (D4 to D7) and other diagenetic products. **(a)** Fibrous dolomite cement (D4) occurs in the D2 matrix surrounded by abundant microbial fabrics, LKG section; **(b)** CL image of D4, with preserved zonation, LKG section; **(c)** bladed dolomite cements (D5) were partially filled in the pores of D3, with associated quartz cement (Q), SA section; **(d)** paragenetic sequence showing D2 followed by pore-filling cements D4 and D6. The host rock is composed of D2, with pre-existing pores occluded by later diagenetic cements D4 and D6, LKG section; **(e)** fine to medium crystalline dolomite cement (D6) and coarse crystalline saddle dolomite cement (D7) partially filled the pores, with D6 overgrown by D7, well QT-1, depth in 6000 m; **(f)** mega-crystalline calcite cement (yellow arrow) and karst breccias (red arrows) in the paleocaves, LKG section, the hammer is 30 cm long for scale; **(g)** a back-scattered electron (BSE) image for mosaic calcite cement (C) with blocky structure, intercrystalline pores (IP) locally occur, SA section; **(h)** bitumen (Bit) locally occurs with the associated columnar stromatolites, SA section, the magnifier is 6 cm long for scale; **(i)** stylolite was filled by bitumen, well LT-1, depth in 8731 m.

suggested that, compared to calcite, dolomite could be more resistant to reordering and may retain primary clumped composition at burial temperatures of up to 150 °C (Lloyd et al., 2018). In this study, the consistent differences in the clumped temperatures ($T_{\Delta47}$) for each measured dolomite component (D1 to D5) match well with the paragenetic sequence, thus implying an insignificant influence of alteration on the calculated $T_{\Delta47}$ during burial diagenesis (Lloyd et al., 2018; Chang et al., 2020). This is supported by the $\delta^{13}C$ and $^{87}Sr/^{86}Sr$ values of most D1 and D2 samples, which are similar to those of coeval seawater (Figs. 7 and 8), indicating that late-stage diagenesis did not substantially modify the original geochemical signals. As for D3, D4, and D5, they exhibit slightly elevated temperatures relative to D1 and D2, possibly reflecting minor diagenetic effects (e.g., recrystallization) on clumped temperatures at greater burial depths (Lukoczki et al., 2020; Fig. 10).

For the late-stage pore-filling cements, two-phase inclusions are more readily observable. Therefore, fluid inclusion microthermometric analysis was employed to determine the formation temperatures of D6, D7, and quartz cements. D6 dolomites (80–117 °C) show significantly higher temperatures than matrix dolomites (D1, D2 and D3) and early-diagenetic dolomites (D4, D5). D7 dolomites yield markedly elevated precipitation temperatures (135–150 °C), while quartz cements range between 110 °C and 130 °C.

5. Discussion

5.1. Paragenetic sequences of dolomite

Dolomite crystals in D1 and D2, which originated from restricted tidal flat facies, are predominantly euhedral with the smallest crystal sizes (2–20 μm), indicating the initial stage of dolomitization at depths shallower than 500 m (Fig. 6; Warren, 2000; Machel, 2004; Lukoczki et al., 2020). Huang et al. (2025) reported the Qigebrak Formation started to deposit in 565 ± 12 Ma. Combined with the burial history (Fig. 3) and the U–Pb dating ages of D1 and D2 (576 ± 16 Ma ~560 ± 26 Ma; Yang et al., 2020b), it could further validate that D1 and D2 were formed

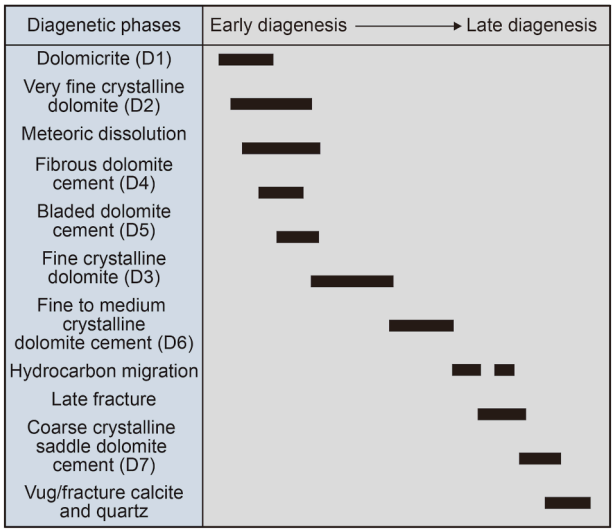

Fig. 6. Paragenetic diagenetic sequence of the Qigebrak Formation.

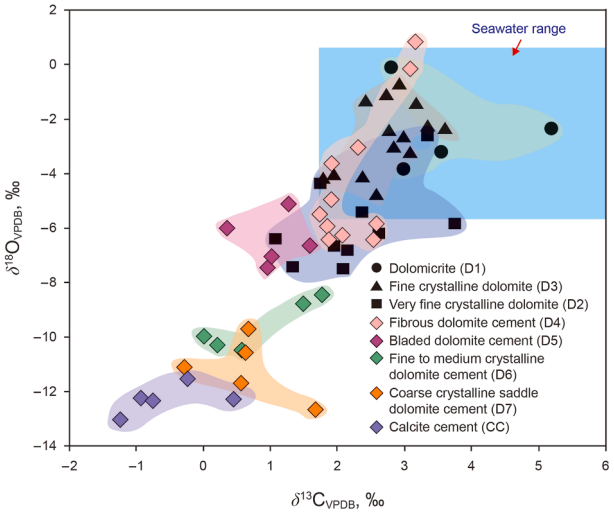

Fig. 7. Carbon and oxygen isotope values of the carbonate minerals in the Qigebrak Formation. The blue rectangle represents coeval seawater isotopic range (He et al., 2007).

from depositional to a very early-diagenetic stage. D3 exhibits relatively small crystal sizes (50–200 μm) but lacks preserved original microbial fabrics, indicating a relatively early shallow-burial dolomitization stage following D1 and D2 (Prather et al., 2023).

Early diagenetic dolomite cements (D4 and D5) are characterized by fibrous and bladed dolomite crystals. The U–Pb ages of D4 and D5 (from 556 ± 17 to 542.7 ± 8 Ma; Shen et al., 2021) are slightly younger than those of the matrix dolomites, yet still fall within the Late Ediacaran period, suggesting near-surface formation (Ding et al., 2019; Hu et al., 2020). D5 commonly overgrows D4 in pores, suggesting that D5 precipitated after D4. D6 and D7 commonly occur in vugs and fractures. The majority of U–Pb ages for D6 dolomites primarily fall within the Ordovician, averaging 472.3 ± 7.7 Ma (Shen et al., 2021). In contrast, D7 dolomites yield significantly younger U–Pb ages of 215 ± 30 Ma, corresponding to the Permian period (Yang et al., 2020b). The non-planar-a D6 is locally cut or overlain by D7 in vugs and fractures (Fig. 5(d)), suggesting that D7 precipitated later than D6, consistent with the U–Pb age of these dolomites.

5.2. Multiphase dolomitization history

5.2.1. Syngenetic dolomitization

As previous study presented, the very fine to fine crystal sizes (2–20 μm) and subhedral to nonplanar textures of D1 and D2, coupled with preserved primary microbial fabrics (Fig. 4(a)–(d)), indicate very early stage diagenesis (Fu et al., 2006). This phase is commonly associated with near-surface dolomitization (Fig. 11; Li et al., 2021c; Ahmad et al., 2022; Rahim et al., 2022; Ning et al., 2024). However, the absence of classical evaporites suggests that the dolomitization occurred in slightly evaporated environments, implying a restricted, low-energy lagoonal or tidal-flat setting (Fig. 12). In this setting, evaporation elevated the Mg^{2+}/Ca^{2+} ratio of seawater, driving dolomite precipitation without attaining gypsum saturation (Tang et al., 2024). Consequently, dolomitizing fluids for D2 likely had salinities below gypsum precipitation levels. Continuous dolomitization in restricted lagoons was sustained by periodic seawater input, facilitating the formation of large-volume D2 (Fig. 12). Furthermore, the common occurrence of microbial fabrics in D2, along with the reported microbial extracellular polymers (EPS) (Zhao et al., 2024), provides direct evidence for microbial activity. This indicates that microbes played a significant role in the initial formation of D2 (Dupraz et al., 2009; Riding, 2011; Bontognali, 2019).

D1 and D2 were formed by slightly evaporitic seawater, which is further supported by geochemical data. Their $\delta^{13}C$, $^{87}Sr/^{86}Sr$ (Figs. 7 and 8) and seawater-like rare earth elements (REE) patterns (Tang et al., 2024) are consistent with those of Ediacaran seawater, indicating that contemporaneous seawater was the primary dolomitization fluid responsible for the formation of D1 and D2 (Bai et al., 2025). In addition, D1 and D2 yield $\delta^{18}O_{water}$ values of 3.09‰–4.90‰ VSMOW for the dolomitization fluids (Fig. 10), which are 8‰–10‰ VSMOW higher than the $\delta^{18}O$ of Neoproterozoic seawater (−5‰ VSMOW; Galili et al., 2019). This also suggests the formation of D1 and D2 was associated with seawater subjected to evaporation. The dolomitization event probably took place at temperatures below 50 °C and depths shallower than 1000 m, as indicated by the lack of two-phase fluid inclusions and the basin burial history (Fig. 3; Gregg and Sibley, 1984; Goldstein and Reynolds, 1994). Thus, D1 and D2 probably formed through reflux dolomitization by slightly evaporative seawater (Fig. 12). Following the syngenetic dolomitization, meteoric water leaching happened at the end of Ediacaran, which was supported by subsequent calcite precipitation (Fig. 5(f) and (g)) with highly negative of $\delta^{18}O$ values (Fig. 7), elevated $^{87}Sr/^{86}Sr$ ratios (Fig. 8) and absence of two-phase fluid inclusions (Zhu et al., 2020).

In the paragenetic sequence, D5 overlies D4, both serving as first-generation cements in microbial-framework pores and solution-enlarged vugs (Fig. 5(a) and c)). Their elongated crystal morphology, predominantly dull to dark-red cathodoluminescence, and frequent occurrence in microbial-framework pores strongly suggest a marine origin (Wood et al., 2017; Hood and Wallace, 2018; Hu et al., 2020; Wang et al., 2020). Additionally, the liquid-only monophase inclusions in D4 and D5 indicate formation in seawater phreatic environments (Fig. 11; Hu et al., 2020). Compared to matrix dolomites (D1 to D3), D4 and D5 exhibit relatively negative $\delta^{13}C$ shifts, suggesting that the meteoric water diagenesis modified these carbonates (Nicolaides, 1997; Shang et al., 2020). The increased $^{87}Sr/^{86}Sr$ ratios in D4 and D5 further suggest the integration of radiogenic ^{87}Sr derived from meteoric water inputs (Xiao et al., 2020).

Table 1
Isotopic data of carbon, oxygen, and strontium for various carbonate minerals.

Samples	Types of carbonate minerals	$\delta^{13}C_{VPDB}$	$\delta^{18}O_{VPDB}$	$^{87}Sr/^{86}Sr$	Error (2s)
17XR-42	Dolomicrite (D1)	5.16	−2.2	0.708835	0.000013
17XR-64	Dolomicrite (D1)	2.98	−3.89	0.708499	0.000012
17SG-62	Dolomicrite (D1)	3.57	−3.31	0.708612	0.000011
18KX-65	Dolomicrite (D1)	2.79	−0.04	-	-
XR-05	Very fine crystalline dolomite (D2)	3.34	−2.35	-	-
XR-07	Very fine crystalline dolomite (D2)	1.88	−4.05	0.708745	0.000012
XR-08	Very fine crystalline dolomite (D2)	1.79	−4.12	-	-
XR-10	Very fine crystalline dolomite (D2)	3.08	−3.28	0.708480	0.000013
XR-12	Very fine crystalline dolomite (D2)	2.77	−2.51	-	-
XR-14	Very fine crystalline dolomite (D2)	2.85	−3.07	0.708477	0.000013
KX-09	Very fine crystalline dolomite (D2)	2.36	−4.14	-	-
KX-10	Very fine crystalline dolomite (D2)	2.93	−0.72	0.708559	0.000011
KX-99	Very fine crystalline dolomite (D2)	3.59	−2.36	-	-
SI-60	Very fine crystalline dolomite (D2)	2.57	−4.79	-	-
SI-66	Very fine crystalline dolomite (D2)	3.18	−1.48	-	-
SG-04	Very fine crystalline dolomite (D2)	-	-	0.708929	0.000011
SG-05	Very fine crystalline dolomite (D2)	2.42	−1.38	-	-
Q3-51-1[a]	Very fine crystalline dolomite (D2)	2.75	−1.64	0.708830	0.000012
Q3-78-1[a]	Very fine crystalline dolomite (D2)	2.97	−2.32	0.708940	0.000012
20XR-04-2-2	Fine crystalline dolomite (D3)	1.79	−4.12	-	-
20XR-05-3	Fine crystalline dolomite (D3)	2.09	−6.78	0.708828	0.000012
20XR-07-1	Fine crystalline dolomite (D3)	2.63	−6.05	-	-
20XR-08-2	Fine crystalline dolomite (D3)	3.34	−2.35	0.708466	0.000014
17SG-85	Fine crystalline dolomite (D3)	1.93	−6.54	0.708675	0.000012
20KX-05-1	Fine crystalline dolomite (D3)	2.41	−5.49	0.708819	0.000014
Well QT-1 (5996.03m)[a]	Fine crystalline dolomite (D3)	2.06	−7.76	-	-
Well QT-1 (5996.73m)[a]	Fine crystalline dolomite (D3)	1.04	−6.3	-	-
Well QT-1 (5996.81m)[a]	Fine crystalline dolomite (D3)	1.36	−7.62	-	-
Well QT-1 (5997.88m)[a]	Fine crystalline dolomite (D3)	3.77	−5.94	0.710063	0.000012
DEG-Z_2q-1-1[a]	Fibrous dolomite cement (D4)	2.6	−5.8	-	-
DEG-Z_2q-1-1[a, b]	Fibrous dolomite cement (D4)	1.91	−6.18	-	-
DEG-Z_2q-1-2[a, b]	Fibrous dolomite cement (D4)	1.98	−6.2	-	-
DEG-Z_2q-1-3[a, b]	Fibrous dolomite cement (D4)	2.57	−6.35	-	-
DEG-Z_2q-1-4[a, b]	Fibrous dolomite cement (D4)	1.89	−6.28	-	-
DEG-Z_2q-4-1[a, b]	Fibrous dolomite cement (D4)	2.29	−3.08	-	-
DEG-Z_2q-3-①[a, b]	Fibrous dolomite cement (D4)	1.90	−5.00	0.708910	0.000006
XH101-12-1-3[a, b]	Fibrous dolomite cement (D4)	3.16	0.86	-	-
XH101-12-2-1[a, b]	Fibrous dolomite cement (D4)	1.92	−3.82	-	-
XH101-12-2-2[a, b]	Fibrous dolomite cement (D4)	1.77	−5.48	0.710000	0.000006
XH101-12-2-3[a, b]	Fibrous dolomite cement (D4)	3.07	−0.16	0.709670	0.000006
KX-121-1	Bladed dolomite cement (D5)	1.27	−5.09	0.708835	0.000013
KX-123-1	Bladed dolomite cement (D5)	0.96	−7.52	-	-
JL16-1	Bladed dolomite cement (D5)	0.35	−6.03	0.709057	0.000012
Q-58-1-1[a]	Bladed dolomite cement (D5)	1.60	−6.61	0.708900	0.000013
Q-58-1-2[a]	Bladed dolomite cement (D5)	1.00	−7.05	-	0.000013
XR-01	Fine to medium crystalline dolomite cement (D6)	0.18	−10.25	0.709268	0.000013
XR-03	Fine to medium crystalline dolomite cement (D6)	0.06	−9.99	0.709444	0.000013
KX-06	Fine to medium crystalline dolomite cement (D6)	-	-	0.709625	0.000013
KX-07	Fine to medium crystalline dolomite cement (D6)	0.57	−10.43	-	0.000011
Q-56-1[a]	Fine to medium crystalline dolomite cement (D6)	1.83	−8.25	-	-
Q-76-1[a]	Fine to medium crystalline dolomite cement (D6)	1.50	−8.77	0.709130	0.000011
KX-123-3	Coarse crystalline saddle dolomite cement (D7)	−0.30	−11.16	-	-
KX-123-2	Coarse crystalline saddle dolomite cement (D7)	0.56	−11.72	-	-
XR-89	Coarse crystalline saddle dolomite cement (D7)	0.67	−9.81	0.709500	0.000013
XR-90	Coarse crystalline saddle dolomite cement (D7)	1.79	−12.64	0.709460	0.000013
XR-91	Coarse crystalline saddle dolomite cement (D7)	0.60	−10.48	-	-
AK-01	Calcite cement	−0.85	−12.31	0.709810	0.000013
AK-03	Calcite cement	−0.89	−12.32	0.709848	0.000010
KX-121-2	Calcite cement	−1.24	−13.02	-	-
KX-121-3	Calcite cement	0.46	−12.14	-	-
KX-121-4	Calcite cement	−0.24	−11.47	-	-

Dashes represent data not measured or unavailable.
[a] Data are collected from Qian et al. (2017), Zheng et al. (2021a, 2021b), and Chen et al. (2023).
[b] Data represent micro-zone geochemical analyses.

5.2.2. Burial dolomitization

Compared to D1 and D2, D3 exhibits coarser crystalline dimensions (Fig. 4(e) and (f)) at greater burial depths. The burial history of the Qigebrak Formation across the Tarim Basin indicates rapid and continuous subsidence after deposition (Fig. 3). Therefore, burial dolomitization has probably occurred under relatively higher temperature conditions. This process likely occurred via recrystallization of pre-existing dolomites or replacement of residual calcite during intermediate burial stage (Machel, 2004). The $\delta^{13}C$ and $^{87}Sr/^{86}Sr$ ratios of D3 are similar to those of early-formed dolomites (D1, D2) (Figs. 7 and 8), suggesting Ediacaran seawater was the primary dolomitizing fluid for D3. This explanation is further supported by the seawater-like REE patterns of D3, which are similar to those of D1 and D2 (Tang et al., 2024). The $\delta^{18}O_{water}$

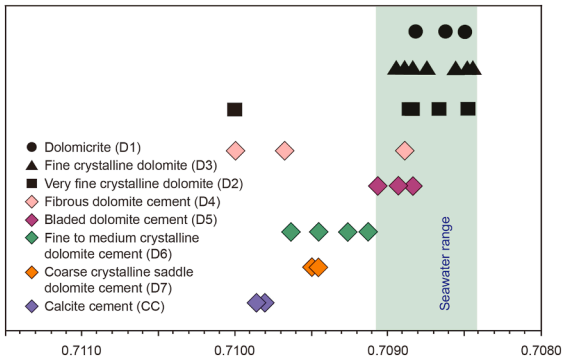

Fig. 8. $^{87}Sr/^{86}Sr$ ratios of dolomite matrix/cement and calcite cement, Qigebrak Formation. Green rectangle shows the seawater range (Zhang et al., 2020).

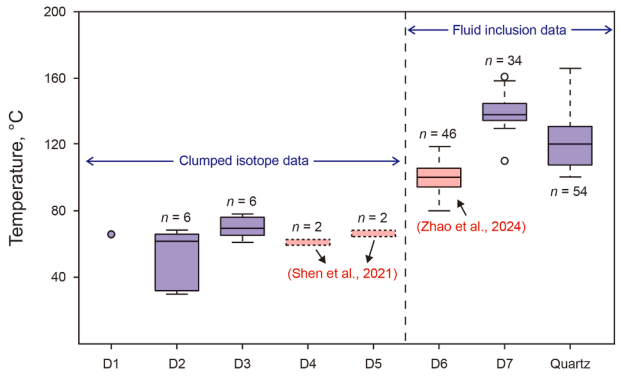

Fig. 9. Temperature data for different types of minerals from the Qigebrak Formation. Pink box plots represent data from Shen et al. (2021) and Zhao et al. (2024), while purple box plots represent newly obtained data from this study.

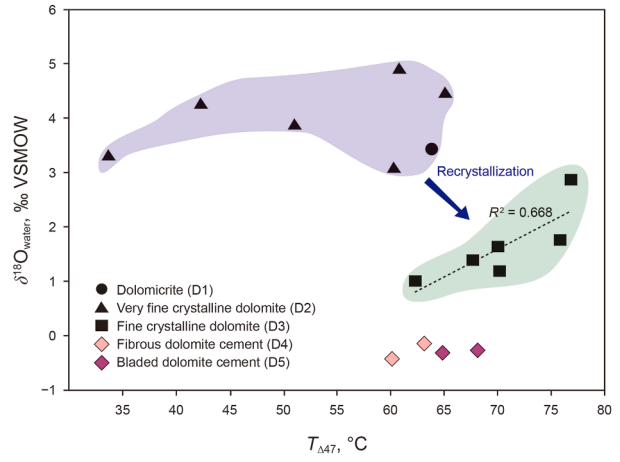

Fig. 10. Relationship between clumped temperatures ($T_{\Delta 47}$) and $\delta^{18}O_{water}$ values from D1 to D5.

values of the dolomitization fluids (0.99‰–2.88‰ VSMOW; Fig. 10) suggest that D3 still exhibits the characteristics of evaporated seawater. However, depleted oxygen isotopes (−7.76‰ to −2.35‰ VPDB) and higher growth temperatures (62–77 °C) confirm D3 formed in burial environments at depths >1000 m (Fu et al., 2006).

D6 commonly occurs as overgrowth cements in the reservoir spaces (Fig. 5(d) and (e)). This dolomite type displays relatively low $\delta^{18}O$ values (−10.43‰ to −8.25‰ VPDB; Fig. 7). Temperature data show these burial diagenetic cements precipitated at 80–117 °C (Fig. 9). Fluid salinity from aqueous inclusions in D6 indicates precipitation from saline waters (5.9–9.6 wt% NaCl equivalent; Fig. 11; Zhao et al., 2024), precluding meteoric water dilution. Thus, D6 originated through burial dolomitization in deep environments buffered by host carbonates. According to the burial history and paragenetic sequences, this dolomitization process probably took place at a depth of 2000–5000 m during the Ordovician to Permian periods. The significantly elevated $^{87}Sr/^{86}Sr$ ratios in D6 (Fig. 8) suggest radiogenic ^{87}Sr incorporation, probably derived from K-feldspar potassium in detrital sediments or deep burial fluids (Jiang et al., 2019).

5.2.3. Hydrothermal dolomitization

Saddle dolomite cements (D7) are commonly present in the Qigebrak Formation, displaying depleted oxygen isotope values ($\delta^{18}O$: −12.64‰ to −9.81‰ VPDB), which differ from those of D4, D5, and D6 (Fig. 7). They have the highest precipitation temperatures (135–150 °C) among all dolomite types. Notably, D6 is locally overgrown by D7 in pores, confirming that D7 formed after D6 under elevated temperatures. Fluid inclusion salinities in D7 are relatively high, indicating more saline dolomitizing fluids than those for D6 precipitation. Moreover, the elevated Sr isotope values of D7 are higher than those of Ediacaran seawater (Fig. 8). This finding, together with the highest diagenetic temperatures among all dolomite types (Fig. 9), suggesting that episodes of deeper and hotter basinal fluids invaded the area (Davies and Smith, 2006), leaching Sr from potassium-bearing rocks (such as mica minerals or clastic sediments containing K-feldspar) during the formation of D7 (Chen et al., 2004; Jiang et al., 2019). The association of high-temperature quartz (Fig. 5(c)) in vugs and pores further supports hydrothermal fluid influence (Koeshidayatullah et al., 2020).

5.3. Effects on reservoir formation

Previous studies have demonstrated that D2 dolostones exhibit superior petrophysical properties compared to D1 and D3, with porosities ranging from 2.5% to 6.0% (Li et al., 2015). Specifically, D2 dolostones supported by skeletal microbial fabrics, such as stromatolites (averaging porosity 4.82%, $n = 24$) and spongiomicrobialite (averaging porosity 6.15%, $n = 32$), display higher porosity (Tang et al., 2022).

As established in prior studies, the Qigebrak Formation in the study area is dominated by large-scale microbial dolomite (D2), and early-diagenetic pores such as microbial-framework pores and solution-enlarged pores are predominant reservoir spaces (Zheng et al., 2021a; Tang et al., 2022). Point count data indicate that microbial-framework pores and solution-enlarged pores of D2 account for 30%–70% of porosity, representing nearly 50% of total porosity in Qigebrak Formation (Tang et al., 2022). As discussed above, these pores are likely formed during an early dolomitization stage under arid climatic conditions (Sun, 1995; Zhu et al., 2020; Ahmad et al., 2022). The pores in dolomite reservoirs are commonly inherited from primary pores, and the dolomitization itself has little contribution to the new-formed pores. Here, we propose that early dolomitization fundamentally controlled the development of these early-diagenetic pores. And the reservoir quality closely linked to two typical dolomitization pathways (Fig. 13).

In the first pathway, pores were dominated by early-stage pores such us primary pores and solution-enlarged pores (Fig. 13(a) and (b)). Burial and hydrothermal fluids may occlude pre-existing pores through mineral precipitation (Fig. 13(c)). Critically, early syngenetic dolomitization (D2) enhances resistance to burial porosity reduction (mechanical/chemical compaction,

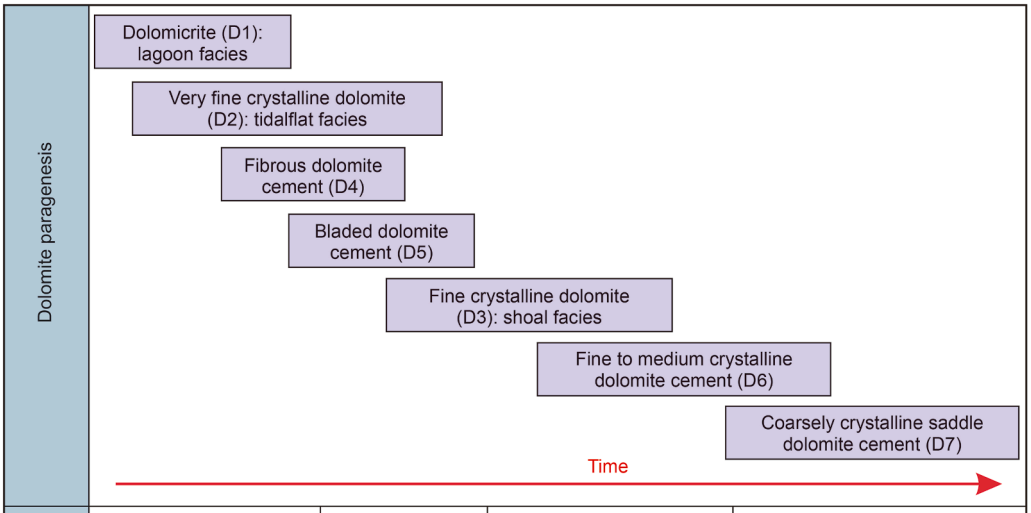

Stages	Stage 1	Stage 2	Stage 3	Stage 4
Models	Syngenetic dolomitization	Burial dolomitization		Hydrothermal dolomitization
	Near surface	Shallow burial	Medium to deep burial	
Fluids	Slightly evaporated seawater, salinity: > 3.5 wt.%	Normal seawater, salinity: ~3.5 wt.%	Influx of burial brine, salinity: 5.9–9.6 wt.%	Influx of burial brine and Sr-enriched hydrothermal fluid, salinity: 9.9–20.1 wt.%

Fig. 11. Schematic diagram showing the dolomite paragenesis in the study area. Diagram illustrating distinct dolomitization models; part of salinity data are from Zhao et al. (2024).

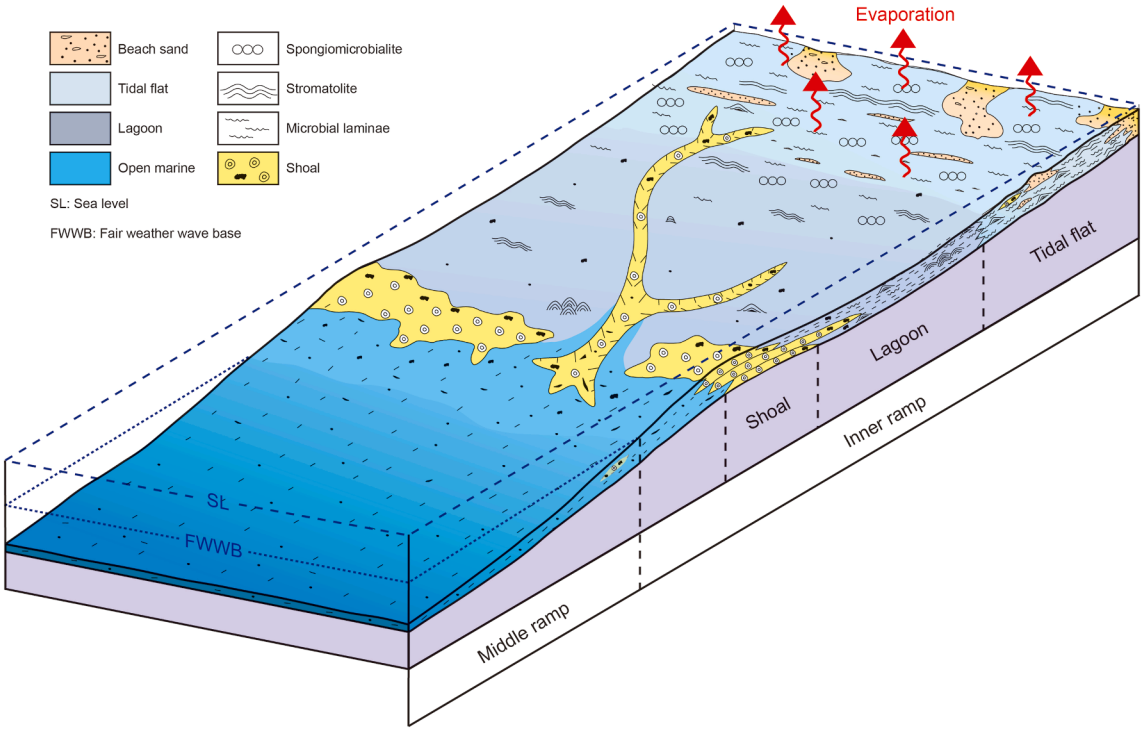

Fig. 12. Schematic model showing the formation of D2 in the Qigebrak Formation, northern Tarim Basin.

cementation) (Schmoker and Halley, 1982), preserving initial porosity. During deposition, abundant microbial textures developed and the rock framework was supported by microbial fabrics (e.g., spongy fabrics; Fig. 13(a)). Subsequent high-frequency sea-level fluctuations during the syndepositional period facilitated the development of framework pores (Fig. 4(d)). This was followed by early syngenetic dolomitization, characterized by the precipitation of a large volume of D2 dolomite (Fig. 13(b)). This process transformed the rock from grain-supported to crystal-supported, significantly enhancing its resistance to burial compaction.

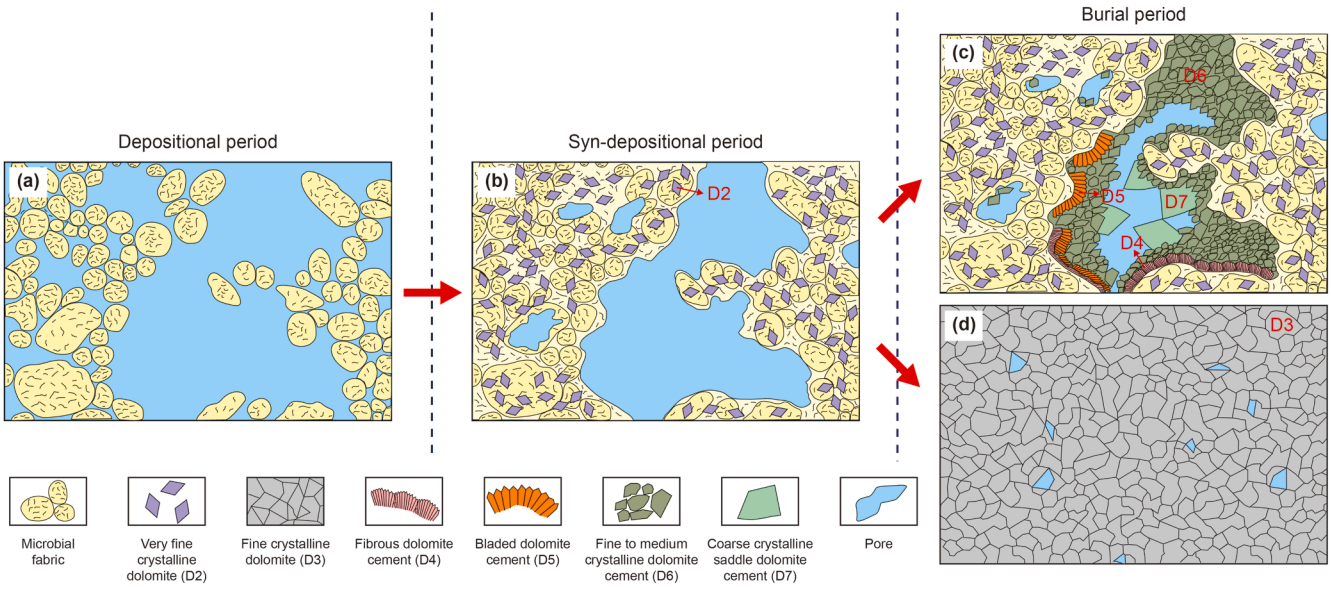

Fig. 13. Pathways of pore evolution in the dolomites of Qigebrak Formation from depositional to burial periods.

Consequently, these primary framework pores remained well-preserved even after prolonged diagenetic evolution in burial environments (Chen et al., 2023). Point count data from thin sections indicate that, even after the cementation of D4 and D5, the D2 dolostones can still possess high porosities exceeding 25%. These observations suggest that syngenetic dolomitization, occurring during very early diagenesis, is likely a key controlling factor for the preservation of primary pores. Similar cases include the Ediacaran Dengying Formation of the Sichuan Basin (Xu et al., 2022), and the Lower Cambrian Xiaoerbrak Formation of the Tarim Basin (Li et al., 2024).

Another pathway involves the modification of pore systems by burial dolomitization (Fig. 13(d)). As reported, intercrystalline pores were likely formed via “mole for mole” replacement or dissolution of calcite or aragonite by dolomite during dolomitization (Machel, 2004; Jiang et al., 2016; Ahmad et al., 2022; Rahim et al., 2022). Even though the intercrystalline pores are commonly presented, particularly in D3 (Fig. 4(f)), the total porosity of this type is less than 10% in the Qigebrak Formation. In summary, while volumetrically minor, intercrystalline pores (Fig. 13(d)) may play a critical role in connecting isolated pores, thereby enhancing overall reservoir permeability (Shen et al., 2024). The composite pore systems in the Qigebrak Formation are dominated by primary pores but are likely enhanced by the connectivity provided by secondary pore networks through burial dolomitization, which adjusts the pre-existing pore systems (Yan et al., 2019).

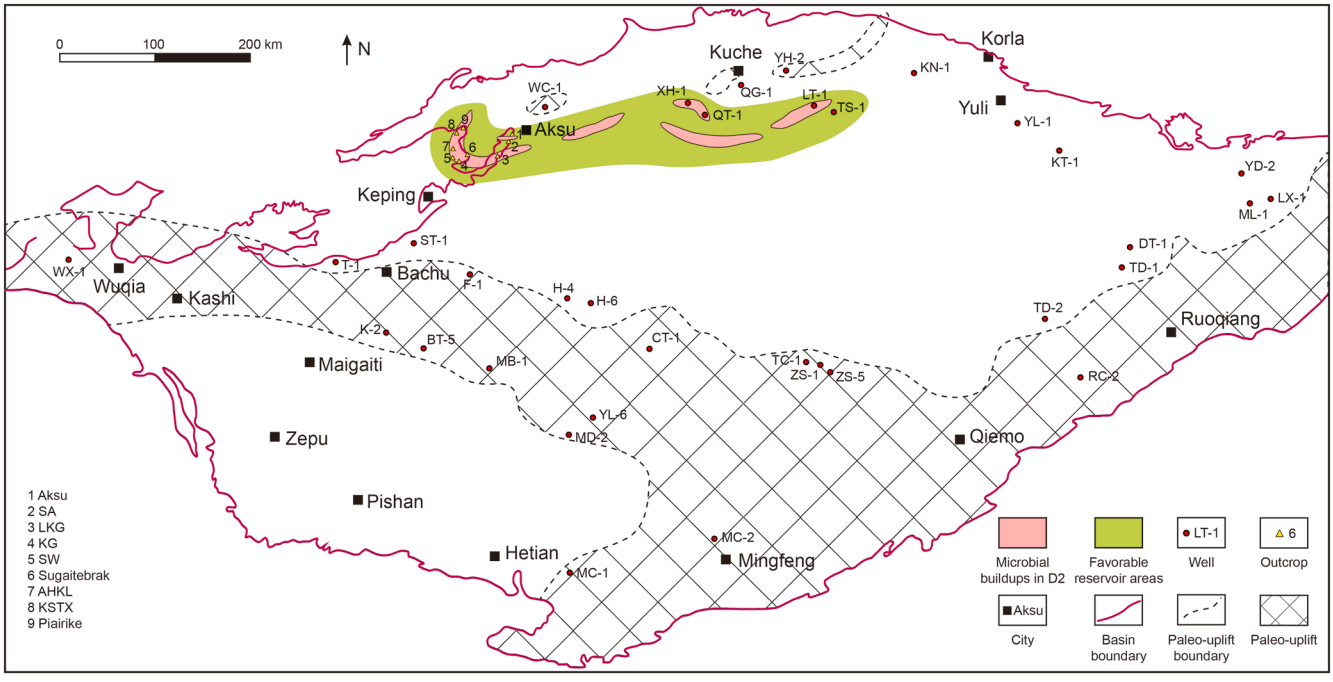

Fig. 14. Favorable reservoir areas of the Qigebrak Formation in the northern Tarim Basin.

Therefore, dolomitization pathways ultimately control the reservoir development in the Qigebrak Formation. The early dolomitization was fundamental to the development of the composite pore systems, with syngenetic dolomitization being the primary factor favoring initial pores preservation (Liu et al., 2020; Shen et al., 2022a; Fig. 13(b)). Additionally, burial dolomitization further improved the previously existing pore systems, with the inheritance of pore systems being more significant than their modification.

5.4. Implications for deep-buried dolomite reservoirs

Hydrocarbon exploration in Precambrian dolomite reservoirs has gained increasing importance in China (Hu et al., 2020; Chen et al., 2023; Liu et al., 2024). Integrating petrology with $\delta^{13}C$, $\delta^{18}O$, $^{87}Sr/^{86}Sr$ isotopic data, coupled with mineral formation temperature data, provides an effective toolkit for constraining the evolution of multistage dolomitizing fluids and evaluating their effects on reservoir development. This study confirms that high-quality deep-buried dolomite reservoirs are primarily controlled by dolomitization pathways, with different pathways exerting distinct influences on pore system development.

Generally, the earlier dolomitization occurs, the better the initial porosity is preserved. Microbial-related rigid frameworks associated with early dolomitization could greatly enhance physical strength and compaction resistance, thereby facilitating the preservation of pre-existing pore networks (Feazel and Schatzinger, 1985; Croize et al., 2013; Zhu et al., 2020). This "fabric-based" preservation mechanism serves as a fundamental control. In contrast, a "pressure-based" mechanism has also been proposed, as documented in the Ediacaran Dengying Formation of the Sichuan Basin (Liu et al., 2022). In such settings, overpressure generated by oil cracking increases pore fluid pressure (Guo et al., 2016). As overpressure intensifies, its porosity-preserving effect strengthens, helping maintain relatively high porosity and permeability and restricting cement production (Duan et al., 2018; You et al., 2020). Overall, however, early dolomitization exerts a more direct and widespread influence on porosity retention by enhancing rock rigidity and limiting compaction, thus fundamentally controlling the preservation of porosity.

This study also implies that the present reservoir spaces in some deep-buried dolomite reservoirs were mainly formed in depositional period and early-diagenetic stage, dominated by primary pores and early-stage dissolution pores. In the study area, high-quality reservoirs are mainly developed in the D2 dolostones of the upper part of the Qigebrak Formation, with a stable thickness of 20–35 m (Yan et al., 2019; Chen et al., 2023). These reservoirs were initially formed by peritidal microbial buildups (e.g., stromatolites, spongiomicrobialites) and later significantly improved by Late Ediacaran meteoric leaching, which was most intense in the Tabei Uplift (Shang et al., 2020). Therefore, favorable exploration targets are areas where D2 microbial buildups overlap with karst modification, primarily in the Tabei Uplift and extending westward to the Keping area (Fig. 14).

6. Conclusions

Based on newly acquired petrographic and geochemical data, this study comprehensively analyzes the nature and evolution of the Upper Ediacaran Qigebrak Formation dolomites in the Tarim Basin. Seven types of dolomite and their corresponding dolomitization models were identified.

Dolomicrite (D1) and very fine crystalline dolomite (D2) represent a very early-stage seawater dolomitization. Fibrous dolomite cement (D4) and bladed dolomite cement (D5) have similar $\delta^{13}C$ and elevated $^{87}Sr/^{86}Sr$ ratios compared to those of D1 and D2, indicating the influence of meteoric water leaching. Petrological and geochemical evidence suggests that D1, D2, D4, and D5 were formed via syngenetic dolomitization in near-surface environments. Fine crystalline dolomite (D3) and fine to medium crystalline dolomite cement (D6) were formed by burial dolomitization and involved mixing burial brine with higher temperatures. Coarse crystalline saddle dolomite cement (D7) represents the final dolomitization stage, attributed to hydrothermal processes.

This study highlights the critical role of early dolomitization in deep-buried carbonate reservoir formation. Early dolomitization enhanced resistance to compaction and pressure solution, and cementation by D4–D7 reduced pore spaces. Although burial dissolution and hydrothermal processes modified these pore systems, present-day pores (6%–8% porosity) primarily inherit from primary and early-diagenetic pores. Thus, early dolomitization is identified as the fundamental factor preserving initial porosity, implying that deep-buried (up to 8800 m) dolomite reservoirs with retained porosity still represent promising petroleum exploration targets.

CRediT authorship contribution statement

Pan Tang: Writing – review & editing, Writing – original draft. **Xiang-Rong Yang:** Conceptualization. **Feng Guo:** Formal analysis, Conceptualization. **You-Jun Tang:** Formal analysis. **Yuan-Zheng Wang:** Conceptualization. **Bo Yang:** Data curation, Conceptualization. **Wen-Yang Wang:** Formal analysis. **Dai-Zhao Chen:** Funding acquisition.

Declaration of interests

The authors declare that they have no known competing financial interests or personal relationships that could have appeared to influence the work reported in this paper.

Acknowledgements

This study was financially supported by the National Natural Science Foundation of China (NSFC, Grant No. 42402158, 42302149, 42572145), the project of Theory of Hydrocarbon Enrichment under Multi-Spheric Interactions of the Earth (THEMSIE04010101), and a scholarship under the Chinese Scholarship Council (CSC) (Grant No. 202510930015). Special thanks to the anonymous reviewers for their constructive suggestions which largely improved the manuscript.

References

Ahmad, I., Shah, M.M., Janjuhah, H.T., Trave, A., Antonarakou, A., Kontakiotis, G., 2022. Multiphase diagenetic processes and their impact on reservoir character of the Late Triassic (Rhaetian) Kingriali Formation, Upper Indus Basin, Pakistan. Minerals 12, 1049. https://doi.org/10.3390/min12081049.

Bai, Z.Z., Shi, S.Y., Hu, Y.J., Yang, W., Xie, W.R., Li, W.Z., 2025. Dolomitization history and porosity evolution of the deeply buried Cambrian Xixiangchi Formation, Sichuan Basin, SW China. J. Palaeogeogr., 100258 https://doi.org/10.1016/j.jop.2025.100258.

Bao, Z.D., Ji, H.C., Wang, Y., Li, Z.F., Liang, T., Niu, B., Wei, M.Y., Lu, K., Shi, Y.Q., Zhang, H., et al., 2022. The primary dolostone in the Meso-Neoproterozoic: Cases study on platforms in China. J. Palaeogeogr. 11, 151–172. https://doi.org/10.1016/j.jop.2022.03.001.

Bernasconi, S.M., Mueller, I.A., Bergmann, K.D., Breitenbach, S.F.M., Fernandez, A., Hodell, D.A., Jaggi, M., Meckler, A.N., Millan, I., Ziegler, M., 2018. Reducing uncertainties in carbonate clumped isotope analysis through consistent carbonate-based standardization. Geochem. Geophys. Geosyst. 19, 2895–2914. https://doi.org/10.1029/2017GC007385.

Bodnar, R.J., 1993. Revised equation and table for freezing point depressions of H2O–NaCl solutions. Geochem. Cosmochim. Acta 57, 683–684.

Bontognali, T.R.R., 2019. Anoxygenic phototrophs and the forgotten art of making dolomite. Geology 47, 591–592. https://doi.org/10.1130/focus062019.1.
Chang, B., Li, C., Liu, D., Foster, I., Tripati, A., Lloyd, M.K., Maradiaga, I., Luo, G., An, Z., She, Z., Xie, S., Tong, J., Huang, J., Algeo, T.J., Lyons, T.W., Immenhauser, A., 2020. Massive formation of early diagenetic dolomite in the Ediacaran Ocean: Constraints on the "dolomite problem". Proc. Natl. Acad. Sci. 117, 14005–14014. https://doi.org/10.1073/pnas.1916673117.
Chang, J., Qiu, N.S., Zuo, Y.H., Li, C.C., 2011. The new evidence on tectonic uplift in Kepingtage area, Tarim Basin: Constraints from (U–Th)/He ages. Chin. J. Geophys. 54, 163–172. https://doi.org/10.3969/j.issn.0001-5733.2011.01.017.
Chen, D., Qing, H., Yang, C., 2004. Multistage hydrothermal dolomites in the Middle Devonian (Givetian) carbonates from the Guilin area, South China. Sedimentology 51, 1029–1051. https://doi.org/10.1111/j.1365-3091.2004.00659.x.
Chen, X.D., Xu, Q.L., Hao, F., Chen, Y.Q., Yi, Y., Hu, F.J., Wang, X.X., Tian, J.Q., Wang, G.W., 2023. Dolomite reservoir formation and diagenesis evolution of the Upper Ediacaran Qigebrak Formation in the Tabei area, Tarim Basin. Sci. China Earth Sci. 66, 2311–2331. https://doi.org/10.1007/s11430-022-1103-4.
Croize, D., Renard, F., Gratier, J.P., 2013. Compaction and porosity reduction in carbonates: A review of observations, theory, and experiments. Adv. Geophys. 54, 181–238. https://doi.org/10.1016/B978-0-12-380940-7.00003-2.
Davies, G.R., Smith, L.B., 2006. Structurally controlled hydrothermal dolomite reservoir facies: An overview. AAPG Bull. 90, 1641–1690. https://doi.org/10.1306/05220605164.
Dennis, K.J., Schrag, D.P., 2010. Clumped isotope thermometry of carbonatites as an indicator of diagenetic alteration. Geochim. Cosmochim. Acta 74, 4110–4122. https://doi.org/10.1016/j.gca.2010.04.005.
Dennis, K.J., Affek, H.P., Passy, B.H., Schrag, D.P., Eiler, J.M., 2011. Defining an absolute reference frame for 'clumped' isotope studies of CO_2. Geochim. Cosmochim. Acta 75, 7117–7131. https://doi.org/10.1016/j.gca.2011.09.025.
Ding, Y., Chen, D.Z., Zhou, X.Q., Guo, C., Huang, T.Y., Zhang, G.J., 2019. Cavity-filling dolomite speleothems and submarine cements in the Ediacaran Dengying microbialites, South China: Responses to high-frequency sea-level fluctuations in an 'aragonite-dolomite sea'. Sedimentology 66, 2511–2537. https://doi.org/10.1111/sed.12605.
Duan, W., Li, C.F., Luo, C., Chen, X.G., Bao, X., 2018. Effect of formation overpressure on the reservoir diagenesis and its petroleum geological significance for the DF11 block of the Yinggehai Basin, the South China Sea. Mar. Petrol. Geol. 97, 49–65. https://doi.org/10.1016/j.marpetgeo.2018.06.033.
Dupraz, C., Reid, R.P., Braissant, O., Decho, A.W., Norman, R.S., Visscher, P.T., 2009. Processes of carbonate precipitation in modern microbial mats. Earth Sci. Rev. 96, 141–162. https://doi.org/10.1016/j.earscirev.2008.10.005.
Feazel, C.T., Schatzinger, R.A., 1985. Prevention of carbonate cementation in petroleum reservoirs. SEPM Special Publ 36, 97–106.
Frolov, S.V., Akhmanov, G.G., Bakay, E.A., Lubnina, N.V., Korobova, N.I., Karnyushina, E.E., Kozlova, E.V., 2015. Meso-Neoproterozoic petroleum systems of the Eastern Siberian sedimentary basins. Precambr. Res. 259, 95–113. https://doi.org/10.1016/j.precamres.2014.11.018.
Fu, Q., Qing, H., Bergman, K.M., 2006. Early dolomitization and recrystallization of carbonate in an evaporite basin: The Middle Devonian Ratner laminite in southern Saskatchewan, Canada. J. Geol. Soc. Lond. 163, 937–948. https://doi.org/10.1144/0016-76492005-088.
Galili, N., Shemesh, A., Yam, R., Brailovsky, I., Sela-Adler, M., Schuster, E., Collom, C., Bekker, A., Planavsky, N., Macdonald, F., Préat, A., Rudmin, M., Trela, W., Sturesson, U., Heikoop, J., Aurell, M., Ramajo, J., Halevy, I., 2019. The geologic history of seawater oxygen isotopes from marine iron oxides. Science 365, 469–473. https://doi.org/10.1126/science.aaw9247.
Goldstein, R.H., Reynolds, T.J., 1994. Systematics of fluid inclusions in diagenetic minerals. SEPM Short. Course 31, 199.
Gregg, J.M., Sibley, D.F., 1984. Epigenetic dolomitization and the origin of xenotopic dolomite texture. J. Sediment. Res. 54, 908–931. https://doi.org/10.1306/212F8535-2B24-11D7-8648000102C1865D.
Grotzinger, J., Al-Rawahi, Z., 2014. Depositional facies and platform architecture of microbialite-dominated carbonate reservoirs, Ediacaran–Cambrian Ara Group, Sultanate of Oman microbialite reservoirs in Oman. AAPG Bull. 98, 1453–1494. https://doi.org/10.1306/02271412063.
Guo, C., Chen, D., Qing, H., Zhou, X., Ding, Y., 2020. Early dolomitization and recrystallization of the lower–middle Ordovician carbonates in western Tarim Basin (NW China). Mar. Petrol. Geol. 111, 332–349. https://doi.org/10.1016/j.marpetgeo.2019.08.017.
Guo, X., Liu, K., Jia, C., Song, Y., Zhao, M., Lu, X., 2016. Effects of early petroleum charge and overpressure on reservoir porosity preservation in the giant Kela-2 gas field, Kuqa depression, Tarim Basin, northwest China. AAPG Bull. 100, 191–212. https://doi.org/10.1306/11181514223.
He, J., Qing, H., Xu, B., 2018. The unconformity-related palaeokarst in the uppermost Ediacaran carbonate rocks in the northwestern Tarim Block, NW China: Implication for sedimentary evolution during the Ediacaran–Cambrian transition. Int. Geol. Rev. 61, 839–852. https://doi.org/10.1080/00206814.2018.1474498.
He, X., Xu, B., Yuan, Z., 2007. C-isotope composition and correlation of the Upper Neoproterozoic in Keping area, Xinjiang. Chin. Sci. Bull. 52, 107–113. https://doi.org/10.1007/s11434-007-0050-2 (in Chinese).
Hood, A.v.S., Wallace, M.W., 2018. Neoproterozoic marine carbonates and their paleoceanographic significance. Glob. Planet. Chang. 160, 28–45. https://doi.org/10.1016/j.gloplacha.2017.11.006.
Hu, Y., Cai, C., Liu, D., Pederson, C.L., Jiang, L., Shen, A., Immenhauser, A., 2020. Formation, diagenesis and palaeoenvironmental significance of upper Ediacaran fibrous dolomite cements. Sedimentology 67, 1161–1187. https://doi.org/10.1111/sed.12683.
Huang, W.W., Zhang, L.L., Zhu, D.C., Liu, L., Li, X.W., Xie, J.C., Wang, Q., Chi, H.Y., 2025. Age constraints on the Ediacaran carbonate carbon isotope excursions in the Tarim Block: Evidence from in situ U–Pb dating of dolostone. Precambr. Res. 418, 107691. https://doi.org/10.1016/j.precamres.2025.107691.
Jia, C., 1999. Structural characteristics and oil/gas accumulative regularity in Tarim Basin. Xinjiang Pet. Geol. 20, 177–183 (in Chinese).
Jiang, L., Cai, C., Worden, R.H., Crowley, S.F., Jia, L., Zhang, K., Duncan, I.J., Hollis, C., 2016. Multiphase dolomitization of deeply buried Cambrian petroleum reservoirs, Tarim Basin, north-west China. Sedimentology 63, 2130–2157. https://doi.org/10.1111/sed.12300.
Jiang, L., Xu, Z., Shi, S., Liu, W., 2019. Multiphase dolomitization of a microbialite-dominated gas reservoir, the Middle Triassic Leikoupo Formation, Sichuan Basin, China. J. Petrol. Sci. Eng. 180, 820–834. https://doi.org/10.1016/j.petrol.2019.05.014.
Jiang, L., Hu, A.P., Ou, Y.L., Liu, D.W., Hu, Y.J., Tang, Y.J., Sun, P., Liu, Y.Y., Wang, Z.C., Cai, C.F., 2023. Diagenetic evolution and effects on reservoir development of the Dengying and Longwangmiao formations, central Sichuan Basin, southwestern China. Pet. Sci. 20, 3379–3393. https://doi.org/10.1016/j.petsci.2023.09.025.
Jin, X., Song, J.M., Liu, S.G., Wang, B., Yang, D., Li, Z.W., Tian, L.Z., Deng, H.S., Ren, S., Xue, J.M., Guo, J.X., Zhang, Z.Y., Shao, X.P., 2025. Coupled effects of paleofluid evolution on ultra-deep microbialite reservoir modification: A case study of the upper Ediacaran Deng-2 member within the Penglai area of central Sichuan Basin, SW China. Pet. Sci. 22, 527–545. https://doi.org/10.1016/j.petsci.2024.10.001.
Koeshidayatullah, A., Corlett, H., Stacey, J., Swart, P.K., Boyce, A., Hollis, C., 2020. Origin and evolution of fault-controlled hydrothermal dolomitization fronts: A new insight. Earth Planet Sci. Lett. 541, 116291. https://doi.org/10.1016/j.epsl.2020.116291.
Land, L.S., 1980. The isotopic and trace element geochemistry of dolomite: The state of the art. In: Zenger, D.H., Dunham, J.B., Ethington, R.L. (Eds.), Concepts and Models of Dolomitization, vol. 28. SEPM, Special publication, pp. 87–110.
Li, F., Deng, J., Kershaw, S., Burne, R., Gong, Q., Tang, H., Lu, C., Qu, H., Zheng, B., Luo, S., Jin, Z., Tan, X., 2021a. Microbialite development through the Ediacaran–Cambrian transition in China: distribution, characteristics, and paleoceanographic implications. Glob. Planet. Chang. 205, 103586. https://doi.org/10.1016/j.gloplacha.2021.103586.
Li, P., Luo, P., Song, J., Jin, T., Wang, G., 2015. Characteristics of Upper Sinian dolostone reservoirs in northwestern margin of Tarim Basin. Mar. Orig. Petrol. Geol. 20, 1–12 (in Chinese).
Li, P., Zou, H., Hao, F., Yu, X., Wang, G., Eiler, J.M., 2021b. Using clumped isotopes to determine the origin of the Middle Permian Qixia Formation dolostone, NW Sichuan Basin, China. Mar. Petrol. Geol. 122, 104660. https://doi.org/10.1016/j.marpetgeo.2020.104660.
Li, P., Zou, H., Yu, X., Hao, F., Wang, G., 2021c. Source of dolomitizing fluids and dolomitization model of the upper Permian Changxing and Lower Triassic Feixianguan formations, NE Sichuan Basin, China. Mar. Petrol. Geol. 125, 104834. https://doi.org/10.1016/j.marpetgeo.2020.104834.
Li, Y., Hu, Y., Cai, C., Zhang, H., Wei, T., 2024. Diagenetic archives of the deeply-buried Cambrian Xiaoerbulake Formation microbialite reservoirs, Bachu–Tazhong area, Tarim Basin, China. Mar. Petrol. Geol. 167, 106987. https://doi.org/10.1016/j.marpetgeo.2024.106987.
Liu, D., Cai, C., Hu, Y., Peng, Y., Jiang, L., 2021. Multistage dolomitization and formation of ultra-deep Lower Cambrian Longwangmiao Formation reservoir in central Sichuan Basin, China. Mar. Petrol. Geol. 123, 104752. https://doi.org/10.1016/j.marpetgeo.2020.104752.
Liu, P.X., Deng, S.B., Guan, P., Jin, Y.Q., Wang, K., Chen, Y.Q., 2020. The nature, type, and origin of diagenetic fluids and their control on the evolving porosity of the Lower Cambrian Xiaoerbulak Formation dolostone, northwestern Tarim Basin, China. Pet. Sci. 17, 873–895. https://doi.org/10.1007/s12182-020-00434-0.
Liu, S., Li, Z., Deng, B., Sun, W., Li, Z., Ding, Y., Song, J., Wu, J., 2022. Occurrence morphology of bitumen in Dengying Formation deep and ultra-deep carbonate reservoirs of the Sichuan Basin and its indicating significance to oil and gas reservoirs. Nat. Gas. Ind. B 9, 73–83. https://doi.org/10.1016/j.ngib.2022.01.001.
Liu, Y., Wang, Z., Ming, X., Jiang, L., 2024. Profitable diagenetic path and reservoir formation efficiency of the Sinian–Lower Cambrian dolostone: Origins of deep dolomites and differential reservoir formation. Acta Sedimentol. Sin. 42, 2159–2173. https://doi.org/10.14027/j.issn.1000-0550.2023.041 (in Chinese).
Lloyd, M.K., Ryb, U., Eiler, J.M., 2018. Experimental calibration of clumped isotope reordering in dolomite. Geochem. Cosmochim. Acta 242, 1–20. https://doi.org/10.1016/j.gca.2018.08.036.
Lukoczki, G., Haas, J., Gregg, J.M., Machel, H.G., Kele, S., John, C.M., 2020. Early dolomitization and partial burial recrystallization: A case study of Middle Triassic peritidal dolomites in the Villany Hills (SW Hungary) using petrography, carbon, oxygen, strontium and clumped isotope data. Int. J. Earth Sci. 109, 1051–1070. https://doi.org/10.1007/s00531-020-01851-7.
Machel, H.G., 2004. Concepts and models of dolomitization: A critical reappraisal. Geol. Soc., Lond. Spec. Publ. 235, 7–63. https://doi.org/10.1144/GSL.SP.2004.235.01.02.
Nicolaides, S., 1997. Marine-derived dolomite in the shallowly buried temperate Port Campbell Limestone (Miocene), Otway Basin, Australia. Sedimentology 44, 143–157. https://doi.org/10.1111/j.1365-3091.1997.tb00429.x.

Ning, M., Wang, Y., McKenzie, J.A., Vasconcelos, C., Li, C., Shen, A., Liang, F., Shen, B., 2024. Dolomite formation during penecontemporaneous subaerial diagenesis: Evidence from modern dolomite crusts forming in lagoon Brejo do Espinho, Brazil. J. Geol. Soc. Lond. 181 jgs2023–j2159. https://doi.org/10.1144/jgs2023-159.

Prather, B.E., Goldstein, R.H., Kopaska-Merkel, D.C., Heydari, E., Gill, K., Minzoni, M., 2023. Dolomitization of reservoir rocks in the Smackover Formation, southeastern Gulf Coast, U.S.A. Earth Sci. Rev. 244, 104512. https://doi.org/10.1016/j.earscirev.2023.104512.

Qian, Y., He, Z., Li, H., Chen, Y., Jin, T., Sha, X., Li, H., 2017. Discovery and discussion on origin of botryoidal dolostone in the upper Sinian in north Tarim Basin. J. Palaeogeogr. 19, 197–210. https://doi.org/10.7605/gdlxb.2017.02.016 (in Chinese).

Radke, B.M., Mathis, R.L., 1980. On the formation and occurrence of saddle dolomite. J. Sediment. Res. 50, 1149–1168. https://doi.org/10.1306/212F7B9E-2B24-11D7-8648000102C1865D.

Rahim, H., Qamar, S., Shah, M.M., Corbella, M., Martín-Martín, J.D., Janjuhah, H.T., Navarro-Ciurana, D., Lianou, V., Kontakiotis, G., 2022. Processes associated with multiphase dolomitization and other related diagenetic events in the Jurassic Samana Suk Formation, Himalayan Foreland Basin, NW Pakistan. Minerals 12, 1320. https://doi.org/10.3390/min12101320.

Riding, R., 2011. Microbialites, Stromatolites, and Thrombolites, Encyclopedia of Geobiology. Springer, Netherlands, pp. 635–654. https://doi.org/10.1007/978-1-4020-9212-1_196.

Schmoker, J.W., Halley, R.B., 1982. Carbonate porosity versus depth: A predictable relation for South Florida. AAPG Bull. 66, 2561–2570. https://doi.org/10.1306/03b5ac73-16d1-11d7-8645000102c1865d.

Shang, Y., Gao, Z., Fan, T., Wei, D., Wang, Z., Karubandika, G.M., 2020. The Ediacaran–Cambrian boundary in the Tarim Basin, NW China: Geological data anomalies and reservoir implication. Mar. Petrol. Geol. 111, 557–575. https://doi.org/10.1016/j.marpetgeo.2019.08.032.

Shen, A., Hu, A., Zheng, J., Liang, F., Wang, Y., 2021. Reconstruction of tectonic-burial evolution based on the constraints of laser in situ U–Pb date and clumped isotopic temperature: A case study from Sinian Qigebrak Formation in Akesu area, Tarim Basin. Mar. Origin Petrol. Geol. 26, 200–210. https://doi.org/10.3969/j.issn.1672-9854.2021.03.002 (in Chinese).

Shen, A., Luo, X., Hu, A., Qiao, Z., Zhang, J., 2022a. Dolomitization evolution and its effects on hydrocarbon reservoir formation from penecontemporaneous to deep burial environment. Petrol. Explor. Dev. 49, 731–743. https://doi.org/10.1016/S1876-3804(22)60306-9.

Shen, A., Hu, A., Qiao, Z., Zheng, J., She, M., Pan, L., 2024. Development and preservation mechanism of deep and ultra-deep carbonate reservoirs. Sci. China Earth Sci. 67, 3367–3385. https://doi.org/10.1007/s11430-023-1417-8.

Shen, W., Zhu, X., Xie, H., Wang, X., He, Y., 2022b. Tectonic–sedimentary evolution during initiation of the Tarim Basin: insights from late Neoproterozoic sedimentary records in the NW basin. Precambr. Res. 371, 106598. https://doi.org/10.1016/j.precamres.2022.106598.

Shi, K., Liu, B., Tian, J., Pan, W., 2016. Sedimentary characteristics and lithofacies paleogeography of Sinian in Tarim Basin. Acta Petrol. Sin. 37, 1343–1360. https://doi.org/10.7623/syxb201611003 (in Chinese).

Shi, S., Liu, W., Huang, Q., Wang, T., Zhou, H., Wang, K., Ma, K., 2017. Dolostone reservoir characteristic and its formation mechanism in Qigebulake Formtion, Sinian, north Tarim Basin. Nat. Gas Geosci. 28, 1226–1234. https://doi.org/10.11764/j.issn.1672-1926.2016.11.006 (in Chinese).

Stolper, D.A., Eiler, J.M., 2015. The kinetics of solid-state isotope-exchange reactions for clumped isotopes: A study of inorganic calcites and apatites from natural and experimental samples. Am. J. Sci. 315, 363–411. https://doi.org/10.2475/05.2015.01.

Sun, S.Q., 1995. Dolomite reservoirs: Porosity evolution and reservoir characteristics. AAPG Bull. 79, 186–204. https://doi.org/10.1306/8D2B14EE-171E-11D7-8645000102C1865D.

Tang, P., Chen, D.Z., Wang, Y.Z., Ding, Y., El-Shafeiy, M., Yang, B., 2022. Diagenesis of microbialite-dominated carbonates in the upper Ediacaran Qigebrak Formation, NW Tarim Basin, China: Implications for reservoir development. Mar. Petrol. Geol. 136, 105476. https://doi.org/10.1016/j.marpetgeo.2021.105476.

Tang, P., Chen, D.Z., Li, S.J., Wang, Y.Z., El-Shafeiy, M., Yang, B., 2024. Early dolomitization mechanism of the Upper Ediacaran Qigebrak Formation, Northwestern Tarim Basin: Evidence from petrography, rare earth elements, and clumped isotope. Minerals 14, 35. https://doi.org/10.3390/min14010035.

Turner, S.A., 2010. Sedimentary record of late Neoproterozoic rifting in the NW Tarim Basin, China. Precambr. Res. 181, 85–96. https://doi.org/10.1016/j.precamres.2010.05.015.

Vahrenkamp, V.C., Swart, P.K., 1994. Late Cenozoic dolomites of The Bahamas: Metastable analogues for the genesis of ancient platform dolomites. In: Purser, B., Tucker, M., Zenger, D. (Eds.), Dolomites, vol. 21. International Association of Sedimentologists, Special Publication, pp. 133–153.

Wang, J., He, Z., Zhu, D., Liu, Q., Ding, Q., Li, S., Zhang, D., 2020. Petrological and geochemical characteristics of the botryoidal dolomite of Dengying Formation in the Yangtze Craton, South China: Constraints on terminal Ediacaran "dolomite seas". Sediment Geol. 406, 105722. https://doi.org/10.1016/j.sedgeo.2020.105722.

Wang, X., Cui, L.L., Li, Y.Y., Huang, X.F., Zhai, J.X., Ding, Z.L., 2016. Determination of clumped isotopes in carbonate using isotope ratio mass spectrometry: Toward a systematic evaluation of a sample extraction method using a static porapak™ Q absorbent trap. Int. J. Mass Spectrom. 403, 8–14. https://doi.org/10.1016/j.ijms.2016.03.008.

Wang, Y., Chen, D., Liu, M., Liu, K., Tang, P., 2022. Ediacaran carbon cycling and Shuram excursion recorded in the Tarim Block, northwestern China. Precambr. Res. 377, 106694. https://doi.org/10.1016/j.precamres.2022.106694.

Warren, J., 2000. Dolomite: Occurrence, evolution and economically important associations. Earth Sci. Rev. 52, 1–81. https://doi.org/10.1016/S0012-8252(00)00022-2.

Wood, R.A., Zhuravlev, A.Y., Sukhov, S.S., Zhu, M., Zhao, F., 2017. Demise of Ediacaran dolomitic seas marks widespread biomineralization on the Siberian Platform. Geology 45, 27–30. https://doi.org/10.1130/G38367.1.

Wu, L., Guan, S., Yang, H., Ren, R., Zhu, G., Jin, J., Zhang, C., 2017. The paleogeographic framework and hydrocarbon exploration potential of Neoproterozoic rift basin in northern Tarim Basin. Acta Pet. Sin. 38, 375–385. https://doi.org/10.7623/syxb201704002 (in Chinese).

Xiao, D., Cao, J., Luo, B., Tan, X., Liu, H., Zhang, B., Yang, X., Li, Y., 2020. On the dolomite reservoirs formed by dissolution: Differential eogenetic versus hydrothermal in the lower Permian Sichuan Basin, southwestern China. AAPG Bull. 104, 1405–1438.

Xu, Z., Lan, C., Zhang, B., Hao, F., Lu, C., Tian, X., Zou, H., 2022. Impact of diagenesis on the microbial reservoirs of the terminal Ediacaran Dengying Formation from the central to northern Sichuan Basin, SW China. Mar. Petrol. Geol. 146, 105924. https://doi.org/10.1016/j.marpetgeo.2022.105924.

Yan, W., Yang, G., Yi, Y., Zuo, X., Wang, X., Lou, H., Rao, H., 2019. Characteristics and genesis of upper Sinian dolomite reservoirs in Keping area, Tarim Basin. Acta Pet. Sin. 40, 295–321. https://doi.org/10.7623/syxb201903004 (in Chinese).

Yang, H.J., Chen, Y.Q., Tian, J., Du, J.H., Zhu, Y.F., Li, H.H., Pan, W.Q., Yang, P.F., Li, Y., An, H.T., 2020a. Great discovery and its significance of ultra-deep oil and gas exploration in well Luntan-1 of the Tarim Basin. China Pet. Explor 25, 62–72. https://doi.org/10.3969/j.issn.1672-7703.2020.02.007 (in Chinese).

Yang, H., Hu, A., Zheng, J., Liang, F., Luo, X., Feng, Y., Shen, A., 2020b. Application of mapping and dating techniques in the study of ancient carbonate reservoirs: a case study of Sinian Qigebrak Formation in northwestern Tarim Basin, NW China. Petrol. Explor. Dev. 47, 1001–1013. https://doi.org/10.1016/S1876-3804(20)60112-4.

You, L., Qu, X., Zhong, J., Li, C., Wu, S., Gao, Y., Cui, J., 2020. Physical simulation experiments on pore evolution in high-temperature and overpressure reservoirs. Nat. Gas. Ind. B 7, 30–39. https://doi.org/10.1016/j.ngib.2019.07.001.

Zhang, C.L., Zou, H.B., Li, H.K., Wang, H.Y., 2013. Tectonic framework and evolution of the Tarim Block in NW China. Gondwana Res. 23, 1306–1315. https://doi.org/10.1016/j.gr.2012.05.009.

Zhang, Y., Yang, T., Hohl, S.V., Zhu, B., He, T., Pan, W., Chen, Y., Yao, X., Jiang, S., 2020. Seawater carbon and strontium isotope variations through the late Ediacaran to late Cambrian in the Tarim Basin. Precambr. Res. 345, 105769. https://doi.org/10.1016/j.precamres.2020.105769.

Zhao, D., Zeng, J., Tan, X., Wang, X., Qiao, Z., Luo, S., 2023. The coupled evolution of depositional systems and paleo-redox conditions was recorded in terminal Ediacaran sedimentary succession in the Tarim Block, NW China. J. Asian Earth Sci. 249, 105623. https://doi.org/10.1016/j.jseaes.2023.105623.

Zhao, D., Ni, C., Li, S., Chen, Y., Qiao, Z., Luo, S., Wang, Q., Tan, X., 2024. Dolomitization history and fluid evolution of end-Ediacaran multi-phase dolomites from the near-surface to deep burial depths in the Tarim craton, northwestern China. Mar. Petrol. Geol. 168, 106929. https://doi.org/10.1016/j.marpetgeo.2024.106929.

Zheng, J.F., Liu, Y., Zhu, Y.J., Liang, F., 2021a. Geochemical features and its geological significances of the Upper Ediacaran Qigeblak Formation in Wushi area, Tarim Basin. J. Palaeogeogr. 23, 983–998. https://doi.org/10.7605/gdlxb.2021.05.063 (in Chinese).

Zheng, J.F., Shen, A.J., Yang, H.X., Zhu, Y.J., Liang, F., 2021b. Geochemistry and geochronology characteristics and their geological significance of microbial dolomite in Upper Sinian, NW Tarim Basin. Acta Pet. Sin. 37, 2189–2202 (in Chinese).

Zheng, J., Wang, H., Shen, A., Luo, X., Cheng, Z., Dai, K., 2023. Genesis of dolomite reservoir in Ediacaran Chigbrak Formation of Tarim Basin, NW China: Evidence from U–Pb dating, isotope and element geochemistry. Minerals 13, 725. https://doi.org/10.3390/min13060725.

Zhou, Y., Yang, F., Ji, Y., Zhou, X., Zhang, C., 2020. Characteristics and controlling factors of dolomite karst reservoirs of the Sinian Dengying Formation, central Sichuan Basin, southwestern China. Precambr. Res. 343, 105708. https://doi.org/10.1016/j.precamres.2020.105708.

Zhu, D., Meng, Q., Jin, Z., Liu, Q., Hu, W., 2015. Formation mechanism of deep Cambrian dolomite reservoirs in the Tarim Basin, northwestern China. Mar. Petrol. Geol. 59, 232–244. https://doi.org/10.1016/j.marpetgeo.2014.08.022.

Zhu, D., Liu, Q., He, Z., Ding, Q., Wang, J., 2020. Early development and late preservation of porosity linked to presence of hydrocarbons in Precambrian microbialite gas reservoirs within the Sichuan Basin, southern China. Precambr. Res. 342, 105694. https://doi.org/10.1016/j.precamres.2020.105694.

Zhu, D., Liu, Q., Wang, J., Ding, Q., He, Z., 2021. Stable carbon and oxygen isotope data of late Ediacaran stromatolites from a hypersaline environment in the Tarim Basin (NW China) and their reservoir potential. Facies 67, 25. https://doi.org/10.1007/s10347-021-00633-0.